ELECTRON DENSITY DISTRIBUTION ANALYSIS BY SR X-RAY DIFFRACTION

– Application to $CaFeO_3$ and ^{13}C Diamond –

A Thesis Submitted to Osaka University

For the Requirements of
the Degree of Doctor of Engineering

Shotaro MORIMOTO

Department of Material Physics
Faculty of Engineering Science
Osaka University

March 1996

ABSTRACT

SR (synchrotron radiation) X–ray diffraction studies are applied to $CaFeO_3$ and diamonds with various concentration of ^{13}C isotope.

The crystalline samples of 0.06 mm used in the study on $CaFeO_3$ were synthesized under 3 GPa and at around 1273 K. The precise structure analyses both in "non–charge–disproportionate" state and in charge–disproportionate state reveal that: (1) the $GdFeO_3$ structure with orthorhombic Pbnm at RT changes a structure of monoclinic $P2_1/n$ with a NaCl type sub–lattice of Fe^{3+} and Fe^{5+} at 113 K; (2) the smaller bond angle of Fe–O–Fe than 180° may weaken the itinerant nature of e_g electrons, break narrow σ^*–band and causes "charge disproportionation" in stead of Jahn–Teller distortion; (3) the negligibly small Jahn–Teller effect in the FeO_6 is explained by the delocalizaion of e_g(Fe) electrons at RT and "disproportionated" state at 113 K; (4) the strong covalent contribution of e_g(Fe) electron and 2p(O) one is suggested by large residual electron density at the middle of the Fe–O bond.

The studies on the diamonds using approximately sphere samples of 0.02 mm reveal the differences due to ^{13}C isotope concentration in the lattice constants, charge density distributions around atoms caused by covalent bonds, and the anharmonicity of thermal vibrations of atoms: (1) the lattice constant varies due to ^{13}C concentration in accordance with the quadratic dependence of $a(X) = 3.56712 - 9.0 \times 10^{-4}X + 3.7 \times 10^{-4}X^2$ Å where X is the atom fraction of ^{13}C; (2) the κ refinements suggest that the valence electron of ^{13}C diamond (98.5(4) wt%^{13}C) slightly shrinks compared to that of natural one (2.0(0.8) wt%^{13}C); (3) the derived 3rd order anharmonic potential parameters indicate that anharmonic thermal vibration to $<\bar{1}\,\bar{1}\,\bar{1}>$ direction is more remarkable than that corresponding to 4th order anharmonicity, and the anharmonicity of natural diamond is slightly larger than that of ^{13}C one.

CONTENTS

ACKNOWLEDGEMENTS

I would like to express my greatest appreciation and gratitude to Professor T. Yamanaka of Osaka University for his continual encouragement and support in coordinating this thesis. I also would like to appreciate Profs. S. Nasu and K. Cho of Osaka University for their kind advice and critical reading of this thesis. I would like to thanks to Prof. R. Oshima of Osaka-prefecture Univ. for his helpful discussion and encouragement. I especially wish to thank Dr. O. Ohtaka for his kind support and encouragement throughout this work. I wish to express my gratitude to Prof. S. Sasaki of Tokyo Institute of Technology for his kind support in structure analysis and Dr. M. Tanaka of KEK-PF for their kind assistance and support in diffraction experiments using SR X-ray.

I am greatly indebted to: Dr. H. Kanda of National Institute of Research in Inorganic Materials for kindly preparing the sample of diamond with various isotope ratio; Prof. E. Ito of Okayama Univ., Prof. R. Kanno and Mr. Sangen of Kobe Univ. for their supports in high-pressure synthesis; Dr. C. Ueda for his help in analysis of isotropic composition of samples by SIMS;

Other thanks are due to all members of Yamanaka Laboratory, and all members of Nasu Laboratory for their helpful discussion and continuous encouragement.

Chapter 1. INTRODUCTION

I. Electron density revealed through X–ray diffraction study

I–1. X–ray diffraction by crystal

Incident X–ray radiation is diffracted elastically from electrons around atoms in the material. Diffraction intensity is proportional to the square of the structure factor which relates to electron density distribution in a crystal through Fourier transformation within the kinematical theory *i.e.* the assumption of the first Born approximation in the scattering theory. A electron density distribution in a crystal revealed through X–ray diffraction study contains the information on chemical bonding in order to understand physical properties of the material. The concept and the importance of an electron density distribution in a crystal through the X–ray diffraction will be described below.

I–2. Basic concept of a structure analysis through X–ray diffraction

A sample for the X–ray structure analysis, a crystal of a sample is considered as an assemblage of perfect crystals with a small distribution in orientation, and with a size (*ca.* 10^3–10^4 Å in length) of a coherent region depending on a wavelength of X–ray. This "mosaic" crystal model represents a real crystal with imperfection which is caused by grain boundaries, dislocations and the other lattice defects. For a mosaic crystal the kinematical theory based on the first Born approximation is available for describing the scattering amplitude of the diffracted X–ray. Within the first Born approximation the interaction between the diffracted beam and the crystal is so weak that the diffracted beam never diffract again in the crystal.

I–2–1. Integrated intensity

Measurement of a diffraction intensity is made by rotating the sample in a small angle around an axis and the intensity at each stepping angle is integrated during the rotation in order to obtain the total intensity of X–ray beam satisfying a diffraction condition. Thus the term of "integrated intensity" is used for the total diffraction intensity obtained experimentally. According to the kinematical theory the integrated intensity, I, of an mosaic crystal is written as follows using the intensity of a monochromatic incident X–ray, I_0, and the absorption factor of the X–ray beam in the crystal, A:

$$I=I_0A \left| \int \rho_{crystal}(\mathbf{r})\exp(i\mathbf{K}\cdot\mathbf{r})d\mathbf{r} \right|^2 (e^2/mc^2)^2LP, \qquad [1.2.1.1]$$

where $\rho_{crystal}(\mathbf{r})$ is the electron density distribution in the crystal at $\mathbf{r}$. $\mathbf{K}$ is the scattering vector. The factor of e^2/mc^2 is the classical Thomson scattering amplitude by a free electron. L is the Lorentz factor depending on experimental arrangement which accounts for the time during the rotating crystal satisfies an diffraction condition and P is the polarization factor of the diffracted beam depending on the polarity of the incident beam.

The electron density distribution in the crystal, $\rho_{crystal}(\mathbf{r})$, is regarded as the 3–dimensional periodic function of the electron distribution in the unit cell, $\rho_{unit\ cell}(\mathbf{r})$. The integral in the equation above is rewritten:

$$\int \rho_{crystal}(\mathbf{r})\exp(i\mathbf{K}\cdot\mathbf{r})d\mathbf{r}$$

$$= \int \rho_{unit\ cell}(\mathbf{r})\exp(i\mathbf{K}\cdot\mathbf{r})d\mathbf{r}\cdot\sum_{hkl}\delta(\mathbf{K}-2\pi\mathbf{g})\cdot N_cV_{crystal}, \qquad [1.2.1.2]$$

where δ is Dirac function, the volume of the crystal, $V_{crystal}$, and the number of unit cells per unit volume, N_c, *i.e.* inverse of the unit cell volume. The

equation above has a finite value where:

$$\mathbf{K} = 2\pi\mathbf{g}, \qquad [1.2.1.3]$$

i.e. "Laue condition" for diffraction is satisfied with **g**, the reciprocal lattice vector as mentioned below.

I–2–2. Structure factor

The Fourier transformation of $\rho_{\text{unit cell}}(\mathbf{r})$ is defined as the structure factor, F, equal to the amplitude of scattering from the unit cell, defined by:

$$F(\mathbf{g}) = \int \rho_{\text{unit cell}}(\mathbf{r})\exp(i\mathbf{g}\cdot\mathbf{r})d\mathbf{r}. \qquad [1.2.2.1]$$

In the definition of the structure factor, $\rho_{\text{unit cell}}(\mathbf{r})$ is considered as a super–position of spherical electrons around isolated atoms for a good approxima–tion. Therefore $F(\mathbf{g})$ can be rewritten as follows:

$$F(\mathbf{g}) = \sum_j f_j \exp(2\pi i\mathbf{g}\cdot\mathbf{r}_j) = \sum_j f_j \exp\{2\pi i(hx_j + ky_j + lz_j)\}, \qquad [1.2.2.2]$$

where f_j is the atomic scattering factor which is the scattering from an isolat–ed atom or ion. Here the set of x_j, y_j and z_j is called the fractional coordinate representing the position, $\mathbf{r}_j$, of the j–th atom in the unit cell as follows:

$$\mathbf{r}_j = x_j\mathbf{a} + y_j\mathbf{b} + z_j\mathbf{c}, \qquad [1.2.2.3]$$

where **a**,**b** and **c** are the basic vectors of the unit cell. h, k and l are the Miller indices indicating the scattering plane and are components of the reciprocal lattice vector, **g**:

$$\mathbf{g} = h\mathbf{a}^* + k\mathbf{b}^* + l\mathbf{c}^*, \qquad [1.2.2.4]$$

where $\mathbf{a}^*$, $\mathbf{b}^*$ and $\mathbf{c}^*$ are the basic vectors of the reciprocal unit cell.

The atomic scattering factor in eq. [1.2.2.2] is the Fourier transforma–tion of the electron density of the j–th atom and is given by:

$$f_j(\mathbf{K})=\int \rho_{j,atom}(\mathbf{r})\exp(2\pi i\mathbf{K}\cdot\mathbf{r})d\mathbf{r}, \qquad [1.2.2.5]$$

$\rho_{atom}(\mathbf{r})$ is calculated theoretically through some techniques of quantum chemistry. The atomic scattering factors widely used are based on the wave functions calculated through the relativistic Hartree–Fock method or the Dirac–Slater method.

Within the first Born approximation for X–ray scattering from an atom, the scattering process is elastic. However, inelastic scattering processes always take place with a finite probability. Thus the atomic scattering factor is complex and dependent of the wavelength of the incident radiation:

$$f = f_0+f'+if'', \qquad [1.2.2.6]$$

where f_0 is the Fourier transformation of $\rho_{atom}(r)$ which is independent of the wavelength; f_0 corresponds to f_j in eq. [1.2.2.5]. The last two terms of f' and f'' are wavelength–dependent and referred commonly to as "anomalous" dispersion terms. The anomalous dispersion is pronounced near an atomic absorption edge.

I–2–3. Atomic temperature factor

Furthermore since an atom is subject to thermal motion at a finite temperature, the elastic scattering intensity should be an average over scattering from all configurations of moving atoms. Within the Born–Oppenheimer approximation, in which the electrons follow perfectly to the motion of the atom, a time–averaged electron density of an atom is considered as the convolution of $\rho_{atom}(r)$ at T = 0 K and a probability distribution function, $P(\mathbf{u})$, of the displacement from the equivalent position of the atom for dis–

placement coordinates, **u**. The Fourier transformation of the average density is the product of the individual functions:

$$< f(\mathbf{K}) > = f(\mathbf{K})T(\mathbf{K}), \qquad [1.2.3.1]$$

where T(**K**), the atomic temperature factor, is the Fourier transformation of the probability distribution, P(**u**). For the simplest example if the thermal motion is assumed to be an 3–dimensional isotropic harmonic oscillation, P(u) is described as follows:

$$P(u) = (2\pi<u^2>)^{-3/2}\exp(-|u|^2/2<u^2>), \qquad [1.2.3.2]$$

where $<u^2>$ is the mean–square displacement in any direction; the atomic temperature factor is expressed as:

$$T(K) = \exp\{-B(|K|/4\pi)^2\} = \exp(-B\sin\theta/\lambda), \qquad [1.2.3.3]$$

where B ($= 8\pi^2<u^2>$) is the isotropic thermal parameter. Anisotropic harmonic oscillation and anharmonic motion are also applicable by taking suitable probability functions.

The expression of the structure factor taking into account thermal motion is in a convenient form as follows:

$$F(\mathbf{g}) = \sum_j f_j T_j \exp\{2\pi i(hx_j+ky_j+lz_j)\}. \qquad [1.2.3.4]$$

As a result the equation for the integrated intensity in eq. [1.2.3.5] is rewritten as follows using the volume of the crystal, $V_{crystal}$, and the number of unit cells per unit volume, N_c, *i.e.* inverse of the unit cell volume:

$$I(\mathbf{g}) = I_0 V_{crystal} A N_c^2 |F(\mathbf{g})|^2 (e^2/mc^2)^2 LP. \qquad [1.2.3.5]$$

I–3. Charge density described by a set of structure factors

The structure factor, F, is the Fourier transformation of the electron

density distribution in the unit cell, $\rho_{\text{unit cell}}(\mathbf{r})$, as expressed in eq. [1.2.1.4]. Thus $\rho_{\text{unit cell}}(\mathbf{r})$ in the crystal can be obtained by inverse Fourier transformation of F. The phases of F are required and should be calculated from a model for charge distribution. Since F has a finite value at discrete reciprocal lattice point due to 3-dimensional periodicity as mentioned above, the integral in the inverse transformation is replaced by a summation of Fourier series as follows:

$$\rho(\mathbf{r}) = (1/V) \sum_{\mathbf{g}} F(\mathbf{g}) \exp\{-2\pi i(hx_j+ky_j+lz_j)\}. \qquad [1.3.1]$$

II. Precise structure analysis using synchrotron radiation (SR) X-ray

II-1. Factors limiting accuracy

Electron density mapping in a crystal needs a set of *accurate* structure. The "structure analysis" assumes a hypothesis of the "ideally imperfect crystal" *i.e.* a positiveness of the kinematical theory in a procedure to derive a structure factor from a set of measured integrated intensity. Thus the accuracy of measured structure factor is limited by the following effects, in addition to experimental errors coming from counting statistics:

(1) *extinction effect* due to the exchange between the incident beam and diffracted beam caused by some "perfection" of the crystal; reducing diffraction intensity from that expected in the kinematical theory

(2) *absorption* of X-ray beam in the crystal; measuring by product of an absorption coefficient and volume for the crystal

Corrections for the above effects on observed intensities should be considered to obtain the set of accurate structure factors. The absorption correction

factor, A, is already appeared in the previous section in eq. [1.2.1.1].

II–2. Extinction effect

Diffraction in the "perfect" crystal is well described by the "dynamical theory" which is at the opposite side of the "kinematical theory". In the dynamical theory the incident and diffracted beams coexist in the crystal and the energy is exchanged between the two beams through diffraction. (This should be compared with no energy exchange between any beams assumed in the kinematical theory.) An important result of the dynamical theory is that the integrated intensity of $I(\mathbf{g})$ specified by a reciprocal lattice vector, $\mathbf{g}$, is proportional to the structure factor, $F(\mathbf{g})$, in contrast to $I(\mathbf{g})$ from the kinematical theory proportional to a *square* of $F(\mathbf{g})$ as seen in eq. [1.2.3.5]. (Note that eq. [1.2.3.5] is on the kinematical theory)

Validity range of the kinematical theory and the dynamical theory is characterized by the "extinction distance", Λ, which has slightly different ways of definition but is of the order of:

$$\Lambda = V_{\text{unit cell}}(a_{\text{Thomson}}|F(\mathbf{g})|\lambda)^{-1} \qquad [2.2.1]$$

where $a_{\text{Thomson}}(= e^2/mc^2)$ is the classical Thomson's scattering amplitude of and $V_{\text{unit cell}}$ is the unit cell volume; When t represents the size of the perfect part; for $t << \Lambda$ the kinematical theory is applicable; for $t >> \Lambda$ the dynamical theory is required (Becker (1977)). It is clear from eq. [2.2.1] that Λ reduces *i.e.* the effect of dynamical diffraction becomes important in case of strong reflections, which is of large $F(\mathbf{g})$, and large wavelength, λ.

Extinction correction on a measured integrated intensity, I, can be ex–

pressed in terms of the intensity expected on the kinematical theory, I_{kin}, which has appeared as **I(g)** in eq. [1.2.3.5] in the previous section:

$$I = y \cdot I_{kin} \qquad [2.2.2]$$

where y is called the "extinction factor" or the "extinction coefficient". The extinction correction in X–ray crystallography is considered by means of the mosaic crystal model composed by many perfect domains, which has appeared in I–2. The extinction effect for the mosaic crystal is separated into primary and secondary extinction effect by the size of the mosaics *i.e.* the perfect domain, r_{domain}; the primary extinction is in the case of $\Lambda << r_{domain}$ and arises from the dynamical effect in each perfect domain; the secondary one is for the contrary case. For synchrotron radiation X–ray from normal bending magnet the extinction factor is simply expressed as:

$$y = y_p \cdot y_s \qquad [2.2.3]$$

where y_p and y_s are the primary and secondary extinction factor respectively; note that such a simplicity comes from the polarization of the incident beam *i.e.* the polarization factor of the unity. Along the line of the treatments of extinction developed by Becker & Coppens (1974) the primary extinction factor is calculated from the solution of an energy transfer equations in the perfect domain, which equations are proposed by Zachariasen (1967), as an first–order approximation because of the difficulties to apply a suitable boundary condition and to obtain the exact solution along the dynamical theory. For the secondary extinction the absence of dynamical effects is assumed in each domain; the extinction is affected by the size or the angular dispersion in the orientation of the domains. Becker & Coppens (1974)

proposed the expression for y_p and y_s in applicable forms to the least-square procedure in a structure analysis; these expressions contain two parameters representing the size and the angular dispersion of domains, which is optimized in the least-square procedure through in a practical ways of a structure analysis.

II-3. Absorption effect

In addition to the extinction effect, absorption of X-ray beam may occur due to photoelectronic process, coherent Rayleigh and incoherent Compton scattering. This absorption effects of the sample crystal is taken account of paths of X-ray beams in the crystal and the linear absorption coefficient, μ; μ depends on the wavelength of X-ray and decreases with decrease in λ but an attention is required near the absorption edges of constituent atoms because of an serious discontinuity of dependence on λ. The absorption effects is evaluated by a product of μ and an effective radius of the crystal, R, defined by cubic-root of the volume; for $\mu R < 0.3$ the absorption should be negligible. For a spherical crystal the absorption factor, A, is simply a function of diffracting (Bragg) angle, θ, for a certain value of μR, which is calculated numerically by Dwiggins (1975).

II-4. Advantage of synchrotron radiation X-ray

The large incident intensity of the synchrotron radiation X-ray makes it possible to increase the accuracy on account of counting statistics because of increase in the observed integrated intensity on account of counting statis-

tics, and also significantly reduces the effects limiting accuracy including those mentioned above (Coppens *et al.* (1992)):

(1) The smaller crystal sample can be used for measurement; it decreases the absorption correction because of decrease in μR, and does the extinction correction because of relatively decrease in the number of mosaic domains.

(2) The beam with the shorter wavelength can be used for measurement; it decreases the absorption extinction correction because of the decrease in the linear absorption coefficient, μ, and increase in the extinction distance.

An additional point still exists. In this study on both $CaFeO_3$ and ^{13}C diamond the sample size is considerably limited by the high pressure devices to synthesize; this requires the source with high intensity to obtain sufficient diffraction intensities.

References

Becker, P. J. (1977). *Acta Crystallogr.* **A33**, 243–49.

Becker, P. J. & Coppens, P. (1974). *Acta Crystallogr.* **A30**, 129–47.

Coppens, P., Cox, D., Vlieg, E. & Robinson, I. K. (1992): "Synchrotron radiation crystallography", Academic, London.

Dwiggins, C. W. Jr. (1975). *Acta Crystallor.* **A31**, 395–6.

Shmueli, U.(*ed.*) (1993): *"Internataional table for crystallography"* Vol.**B**, Kluwer Academic, Dordrecht.

Zachariasen, W. H. (1967). *Acta Crystallor.* **23**, 558–64.

Chapter 2. APPLICATION to $CaFeO_3$

I. Introduction

I–1. Crystal chemistry of perovskite compounds

The "perovskite" is one of the general names of structures referring to the compounds with chemical formula ABX_3, and has taken after the name of the natural mineral oxide of calcium titanate, $CaTiO_3$. In a formula ABX_3, A and B are cations and X is an anion, typically oxygen or fluorine (Fig. 1.1). A few compounds having a sulphur and a chlorine as an anion are also known. Generally, the cation A and the anion X have similar size in their empirical ionic radii, which are defined from statistical bond lengths by Shannon(1976), while the cation B has a small size. Since perovskite structure is a "tolerant" structure, there is a wide variety of combinations for A and B cations leading many kinds of structural modifications or polymorphs.

Perovskites can be classified according to their symmetries. The ideal form of perovskite is quite simple and belongs to space group $P\bar{m}3m(O_{h1})$(No.221) in the cubic system. The unit cell of the cubic perovskite contains one ABX_3 formula unit. The BX_6 octahedra are arranged in a regular fashion sharing X anion at vertices of each octahedron. The A counter–cation at the center of space between the octahedra is coordinated by twelve X anions. The Goldschmidt tolerance factor, t, is proposed for a measure for "tolerance" of perovskite structure, and it is a guide for a combination of A, B and X elements which can construct perovskite structure. The factor is expressed as follows:

$$t = (r_A + r_O)/\sqrt{2}(r_B + r_O), \qquad [1.1.1]$$

where r_A, r_B and r_X are ionic radii for A, B and X ions respectively. The ideal

value of t is unity. The combination of three elements whose t deviates from unity constructs a distorted perovskite structure.

Perovskites with a distortion from the cubic form have tetragonal, orthorhombic, rhombohedral and monoclinic symmetry. Structural modification of perovskite from cubic structure to other structures with lower symmetry can be caused by following reasons:

(1) Displacements of the cations (A and/or B) along certain directions.

(2) Tilting versus a certain direction parallel to the crystallographic axes of the cubic un-tilted perovskite of the BX_6 octahedra (or rotating around a certain axis of the BX_6 octahedra).

(3) Elongation along certain directions of BX_6 octahedra through electron-phonon interaction, for example, the Jahn-Teller effect.

(4) Combination of the above three.

Glazer(1972 & 1975) classified perovskite structures based on the tilting of BX_6 octahedra, which is the second term in the list mentioned above, and demonstrated the relation between modes of tilting and space groups of the structures. Some modes of tilting cause structures being required larger unit cell with two or more formula units for the repetition of symmetry.

If the A counter-cation is too large to be accommodated at the center of the vacant space made by the four BX_6 octahedra, some hexagonal polymorphs are formed. In these polymorphs, some close-packed AX_3 layers stack in the hexagonal form, while in cubic perovskite, all layers do in the cubic form along their <111> direction. The BX_6 octahedra share their corner at cubic stacking of AX_3 layer and the octahedra share their triangle faces at

hexagonal stacking. A wide variety of polymorphs is possible on the line between cubic stacking and hexagonal stacking. The hexagonal perovskites are classified by the periodicity of AX_3 stacking.

Cation orderings at A or B–site in perovskites, such as $A_2(B'B'')X_6$, $A_3(B'_2B'')X_9$, $A_4(B'_3B'')X_{12}$, etc. are known for two different ions at B–site of perovskite and $(A'_3A'')B_4O_{12}$ for two different ions at A–site. Ordering of B' and B" at B–site will require a new unit cell with volume larger than that of original one and change the space group of appearing structure. That is the same fashion at A–site. Note that these structures are not perovskite strictly but superstructures of perovskite.

A certain amounts of cation or anion defects can be introduced to the perovskite structure. Sometimes perovskites with cation defects are seemingly interpreted as anion excess perovskites. Some anion defects ordered phases are known for example as demonstrated for the $Ca_2Ti_{2-2x}Fe_{2x}O_{6-x}$ system by Grenier *et al.* (1970).

I–2. Interests in physical properties of perovskites oxides

Even before the discovery of high–T_c oxide superconductors since Bednorz & Müller (1986), there had been paid much attention on perovskites and perovskite–related oxides because of [a] their physical properties of industrial importance, such as pyro– and piezo–electricity, dielectric susceptibility, linear and non–linear electrooptic effects, [b] a their wide range of electrical resistivity as insulator semi–conductor, metallic conductor to superconductor such as $Ba(Pa_{1-x},Bi_x)O_3$ with T_c = 13 K (Sleight, Gillson &

Bierstedt (1975)), [c] magnetic properties of non–, Pauli–para–, ferri–, anti–ferro– and ferro–magnetism.

I–3. Oxides with 3d transition metal ions with unusual valence states

Oxides system with K_2NiF_4 structure containing octahedrally coordinated Cu^{3+} and Ni^{3+} with higher valences are intensively studied by Demazeau *et al.* (1984). A high valence state of Fe^{6+} is prepared by wet method but their physical characters are not clarified.

Fe^{4+} is encountered even at ambient oxygen pressure in the system of $SrFeO_{2.5+\delta}$, in $SrFeO_3$ at 600 atom in oxygen partial pressure. Fe^{4+} in $CaFeO_3$ is fixed only in the higher oxygen partial pressure, in usual, than 2 GPa with the help of a high pressure apparatus.

Fe^{4+} in $CaFeO_3$ shows disproportionation reaction into two kinds of electronic states which are assigned as Fe^{3+} and Fe^{5+} at low temperature revealed by its Mössbauer spectrum (Takano *et al.* (1977), Nasu *et al.* (1992)) in spite of that in $SrFeO_3$ its valence is kept down to 4.2 K (Mac–Chesney *et al.* (1965)) (Fig. 1.2). This "charge disproportionation" is a very unique feature of Fe^{4+}.

I–4. Purpose

As is known, after the excitements of high–T_c superconductor since 1986 (Bednorz & Müller (1986)), perovskite and perovskite–related oxides especially containing transition metal cation have been paid special attention. To understand the mechanism of high–T_c superconduction, the relation

between electronic state of transition metal cation and its electrical transport property or magnetic property should be made more clear and reconsidered with special care. Perovskites can be the best and simplest example for understanding electronic states of 3d transition metal and appearing physical property.

The structure analysis gives a great information on chemical bonds and physical properties. There are many compounds which have been believed to be perovskites, but even on the natural perovskite its precise structure has been confirmed in recent years (Sasaki *et al.* (1983)), hence there should be reconsideration even on the structural aspect of perovskites as was pointed out by Glazer (1972 & 1975) of the classification of perovskite structure from the view point of tilting octahedra. Thus a precise structure analysis are also needed for already known or unknown perovskites and perovskite-related oxides

As was pointed out by Bednorz and Müller (1986), the presence of Cu^{2+}, which is so called Jahn–Teller ion, plays a lager part in changing to high–T_c superconductivity from bipolaronic insulation with one hole at e_g orbital in octahedral oxygen environment showing the Jahn–Teller effect *i.e.* strong electron–phonon interactions in oxides.

The octahedrally coordinated Fe^{4+} in the high spin state having $(3d)^4$ electronic configuration provides cooperative Jahn–Teller effects. Thus strong electron–phonon coupling is anticipated in the system containing Fe^{4+}.

In the system of high–T_c superconductor, 3d electron levels of Cu cation are lower than 2p levels of O anion. Consequently, holes are intro–

duced not in 3d levels of Cu but in 2p levels of O. Coupling of these holes forming a Cooper pair is one of the most possible explanations of superconductivity in the cuprates system. Since 3d levels of Fe cation become lower as increasing its formal valence, it is expected that 3d levels of Fe^{4+} overlap with 2p levels of O. Thus holes are induced not in 3d levels but in 2p levels; this situation is very similar to the high–T_c superconductor.

$CaFeO_3$ is a special material in the category of perovskite structure, oxide system containing 3d transition metal ion with unusual valence state and a system exhibiting a charge disproportion. However, precise structural aspect including its charge density distribution has not been elucidated. This is the major motivation of this study.

II. Experimental

II–1. Sample synthesis

$CaFeO_3$ with unusual Fe^{4+} ion can be only synthesized under high oxygen partial pressure. This material is produced by following reaction (*cf.* Fig. 2.1):

$$Ca_2Fe_2O_5 + 1/2O_2 \rightarrow 2CaFeO_3 \qquad [2.1.1]$$

$CaFeO_{2.5}(Ca_2Fe_2O_5)$ with the brownmillerite (Ca_2FeAlO_5) structure (Fig. 2.2) is classified as oxygen defect perovskite. Annealing the sample under high oxygen partial pressure can reduce the oxygen defects. Applying high pressure makes it easy to introduce oxygen atoms in the crystal lattice, because oxide perovskite structure is more stable under higher pressure.

Starting material and oxidizer were charged in the gold capsule. To prevent from direct reaction of the former and the latter, zirconium dioxide disk was inserted between them. A sample was synthesized in the capsule under appropriate pressure and temperature, and it was held at the pressure range from 2 GPa to 4 GPa and temperatures in the range between 1223 K and 1473 K for suitable reaction time in the range from 30 min to 36 hrs.

Starting material $CaFeO_{2.5}(Ca_2Fe_2O_5)$ was prepared by means of solid state reaction: A pellet of the mixture of reagent α–Fe_2O_3 (Nakarai tesque Co. Ltd. 99%) dried at 1273 K in air and $CaCO_3$ (Nakarai tesque Co. Ltd. 99%) dried at 383 K in air was calcined at appropriate temperature and reground well after calcination. This procedure of calcination and regrind was repeated three times: in the first stage the pellet was heated at 1173 K for 6 hrs., in the second at 1273 K for 6 hrs. and in the final stage at 1423 K for

over 12 hrs. The brown powder was obtained after the final calcination and was confirmed as single phase of $CaFeO_{2.5}$ by X–ray diffractometer(XRD) using Cu–Kα radiation.

Four kinds of oxidizer were used: three kinds of reagents of $KClO_4$, KIO_3 and CrO_3 (Nakarai tesque Co. Ltd.) and synthesized CaO_2. All of the oxidizers release oxygen by their thermal decomposition below *ca.* 923 K. CaO_2 was synthesized as follows. $CaO_2 \cdot nH_2O$ was precipitated from an aqueous saturated solution of calcium hydroxide ($Ca(OH)_2$) by adding an aqueous solution of hydrogen peroxide (H_2O_2). White powder CaO_2 was obtained after drying this precipitation at 403 K for over 1 day. XRD pattern shows broad peak due to fine crystallite particle size with weak additional peak of co–existing hydrate phases.

Two types of high pressure apparatus were employed in the present experiments. One was the cubic anvil type apparatus which can generate pressure up to 6 GPa (Fig. 2.3(a)). This apparatus has six anvils of sintered tungsten carbide truncated as a form of regular square with 10 mm sides. The cell assemblage for this apparatus was shown Fig. 2.4(a). Sizes of the cap–sules were *ca.* 5 mm tall and 3 mm in diameter. Weight of the recovered sample was *ca.* 10 mg per run. Pressure was estimated from the calibration curve versus loaded pressure based on the two transition pressures of Bi I–II (2.55 GPa) and Ba I–II (5.5 GPa) which were decided by change in electrical resistivity. The other device was the piston cylindrical device which can generate pressure up to 3 GPa. This cylinder and piston were made by sin–tered tungsten carbide. The detailed cell assemblage for this device is shown

in Fig. 2.4(b). The capsule of *ca.* 10 mm tall and 5 mm in diameter was used. 100 mg sample was recovered per run. Pressure was estimated by cross section ratio of a piston to the pressure ram and loaded oil pressure. A graphite tube heater was employed to elevate temperature in both systems. Temperature was monitored by Pt–Pt13%Rh thermo–couple during the run.

Recovered powder samples were characterized by means of XRD and electron probe micro analysis (EPMA). XRD measurements were performed by Rigaku RAD–B diffractometer using Cu–Kα radiation from a sealed X–ray tube. This diffractometer has a pyrolytic graphite monochromater just in front of the scintillation counter in order to eliminate the Kβ radiation and a fluorescent X–ray. The step scan mode measurement was employed in which the step width was 0.02° deg. and scanning speed was 1 sec/step.

The chemical compositions of recovered samples were analyzed with JEOL JXA–733 X–ray micro analyzer from the intensity ratio of the characteristic X–ray by application of atomic–number, absorption and fluorescence (ZAF) corrections.

Thermal stability of the sample analyzed by TG(Thermo–Gravimetry)–DTA(Differential Thermal Analysis) with Al_2O_3 as a reference. $CaFeO_3$ releases their oxygen and becomes $CaFeO_{2.5}$ at 1273 K. XRD patterns of the sample were also measured after being kept at an desired temperature in a range of from 373 K to 473 K.

Electrical resistivity measurements were performed on sintered pellets whose dimensions were *ca.* 4 mm x 3 mm x 1 mm by means of the four–probe method in a temperature range from 35 K to 293 K. A constant dc

current in a range from 0.1 mA to 10 mA was supplied to the sample in the measurements. The electrical resistivity of the sample was calculated by following equation:

$$\rho = (V/I)(S/l), \qquad [2.1.2]$$

where V is a voltage measured by two electrodes, I is a supplied dc constant current, S is a cross section area of the sample and l is a distance between the two electrode monitoring voltage.

^{57}Fe Mössbauer spectra of the powder sample were obtained in transmission geometry at room temperature. A velocity range in the measurements are from −10 to +10 mm/sec. Doppler velocity is calibrated by the magnetic hyperfine splitting of Fe metal as a reference. Isomer shift of a sample is measured in reference to that of a metal iron as zero.

II–2. Crystal Structural analysis

Cube–shaped crystalline sample with edge size in a range from 60 μm to 200 μm were selected to take X–ray diffraction photographs by means of the precession camera. The Mo Kα radiation from sealed X–ray tube was used without Kβ filter. The precession camera can make it possible to get a image of any reciprocal lattice plane without any deformation in contrast to the Weissenberg camera.

A single crystal with a size of 60 μm was selected for single crystal diffractometry at 293 K and 113 K which is low enough to exhibit the charge disproportionation of iron ion. Single crystal structure refinement has been performed by synchrotron radiation. The vertical four–circle diffractometer

installed in beam–line 10A at the Photon–Factory was used (Fig. 2.5 and Fig. 2.6). Intensity of incident radiation emitted from a normal bending magnet decreases gradually as decrease in the number of positron in the storage ring. This storage ring was operating at 2.5 GeV with ring current of 300 mA soon after the injection of positron. The incident radiation used was monochromated by a monolithic Si(111) crystal. The observed diffraction intensity could be well normalized referring to the intensity of standard reflections which was corrected every 20 reflections. The accurate value of wavelength of λ = 0.69848(3) Å used was determined by the observed dif–fraction angles from a standard ruby (Al_2O_3) crystal. Lattice parameters and setting parameters (UB–matrixes) at 293 K and 113 K were determined from 25 reflections between $70° \leq 2\theta \leq 90°$. The obtained setting parameters were well describing observed reciprocal lattice points. The deviations in miller index of each reflection were within 0.003. after indexing of observed reflec–tions.

After intensity normalization for the decreasing of incident intensity because of current decay, integrated intensities were corrected for Lorentz and polarization correction to derive the observed kinematical structure factor of each reflection. These structure factors can be scaled to the absolute values in a refinement procedure. The polarization factor was assumed to be unity because the radiation from normal bending magnet without any insertion device was regarded as fully polarized light in the plane of the positron orbit in the storage ring.

In addition to a scale factor to obtained absolute values of the observed

in the storage ring.

In addition to a scale factor to obtained absolute values of the observed structure factors, fractional coordinates and isotropic temperature factors of atoms are refined to minimize differences between the set of the observed structure factors and the set of the calculated ones in least square procedures of structure refinements. All strucutre refinements were carried out with RADY developed by Sasaki (1987) on a personal computer.

Charge density distribution was studied by means of the difference Fourier synthesis based on the difference between the observed strucutre factors and a calculated ones obtained after a refinement procedure. The difference Fourier synthesis reveals a deformation charge density, $\Delta\rho(\mathbf{r})$, from the model density demonstrated by a refined set of strucutre factors:

$$\Delta\rho(\mathbf{r}) \equiv (1/V) \sum_{\mathbf{g}} [F_{obs}(\mathbf{g}) - F_{calc}(\mathbf{g})]\exp(-2\pi i\mathbf{g}\cdot\mathbf{r}), \qquad [2.1.3]$$

where F_{obs} and F_{calc} are the observed and the calculated structure factors respectively.

The positiveness of a refinement is measured by the weighted R–factor, $R_w(F)$, defined by:

$$R_w(F) \equiv \{ \Sigma w(|F_{obs}| - |F_{calc}|)^2 / \Sigma w|F_{obs}|^2 \}^{1/2}, \qquad [2.1.3]$$

where w is the weight assigned to each reflection and the sums are over all sets of the relections used in the refinement.

III. Results

III–1. Sample synthesis

Single phase of $CaFeO_3$ was obtained after applying above 2GPa and at 1223K. The amounts of the desired phase is very sensitive to the synthesis pressure and/or temperature, especially to the temperature. The products recovered under unsuitable pressure and/or temperature show additional peaks in their XRD powder patterns. Note that the most of additional peaks were sharp and cannot be explained as the starting material $CaFeO_{2.5}$.

At higher temperature chemical reaction is more enhanced. In the case of synthesis of $CaFeO_3$, however, application of higher temperature failed to synthesize a single phase of $CaFeO_3$. This suggests that a deoxidization of $CaFeO_3$ should be dominant comparing for a oxidization of $CaFeO_{2.5}$ at the temperature.

The condition to synthesize $CaFeO_3$ in this work has satisfied following requirements:

(1) pressure is high enough to hold oxygen partial pressure $p(O_2)$ which can stabilize Fe^{4+};above 2 GPa and under the appropriate pressure as above.

(2) temperature is high enough to decompose CaO_2 and release O_2 gas; this was confirmed by a recovered product of CaO fully decomposed in the reaction container.

(3) temperature is high enough to oxidize of $CaFeO_{2.5}$ and to form $CaFeO_3$.

(4) temperature is lower than that of the deoxidization of $CaFeO_3$ into

$CaFeO_{2.5}$.

It has been known that oxides containing ferric or ferrous ions display various color from red or brown to deep purple. The color of these oxides depends on the valence state of iron ion and is very sensitive to grain size. Powder sample prepared in a proper way shows a black color, while the starting material $Ca_2Fe_2O_5$ shows a brown color. $CaFeO_3$ seems to be black independently of their grain sizes from a few μm to a few hundred μm which sizes appear in these synthesis experiments. This means that black $CaFeO_3$ powder shows their intrinsic color and it is regarded as the characteristic color of tetravalent iron ion(Fe^{4+}). This is also in accordance with the facts that $SrFeO_3$ also containing Fe^{4+} seems black. The most probable suggestion for the colors of $CaFeO_3$ and $SrFeO_3$ is that rapid electron transfer occurs between iron cations one another through a ligand of oxygen anion. This is in accordance with both the semi-conducting behavior of $CaFeO_3$, as mentioned below, and the metallic one of $SrFeO_3$ (Nagata and Kanno (1994)) in temperature dependence of electrical conductivity.

Grain size of recovered sample was examined preliminary with an optical microscope. An application of $KClO_4$ or KIO_4 as a oxidizer make grain size small as a few μm, while that of CaO_2 makes it large as a few hundred μm. Then single crystals of the large size enough to use for structure analysis were synthesized successfully only in the case using CaO_2 as a oxidizer. Crystal growth of $CaFeO_3$ is enhanced by the following reasons in addition to the suitable pressure and temperature:

(1) large volume of the reaction container, which is most commonly

required in crystal growth; the piston cylindrical device is recommended.

(2) higher pressure than the critical one of 2 GPa; equal to or above 3 GPa is desired for $CaFeO_3$, which has an upper-limit due to the volume of container.

(3) some moisture atmosphere which plays a similar part to a flux in the container under the pressure and temperature applied; the precipitates of CaO_2 as the oxidizer is a good choice.

Thermal stability of samples was examined by means of TG-DTA. The products after heating in the TG-DTA measurement are deoxidized into the starting material of $CaFeO_{2.5}$ completely, which is confirmed through powder XRD. $CaFeO_3$ released its oxygen above 600 K in elevating temperature at ambient pressure.

As mentioned above in the experimental section, a sample was recovered as a well sintered pellet by high pressure and high temperature treatment. It was suitable for measurements of electrical resistivity. Electrical resistivity of $CaFeO_3$ as a function of temperature is shown in Fig. 3.1 in the range from room temperature(293 K, RT) to 35 K. The resistivity ρ of a sample was *ca.* 5×10^{-1} Ωcm at RT and was within a category of semiconductivity. It is relatively lower than the typical value of metallic oxides that is $> 10^{-4}$ Ωcm and higher than the typical value of oxides in a category of insulator that is $< 10^{10}$ Ωcm. The semiconductive character of $CaFeO_3$ was indicated by its temperature dependence of increasing resistivity as decreasing temperature. The activation energy was estimated from the inclination on

Arrhenius plot of ln(ρ) versus reciprocal of T. The estimated activation energy was *ca.* 0.1 eV. Note that the absolute value of electrical resistivity in these measurements is less accurate because of difficulty to estimate the accurate values of cross section of the samples. Their size cannot be well controlled. The semiconductive feature of $CaFeO_3$ was, however, well confirmed since the temperature dependence of resistivity is still reliable.

^{57}Fe Mössbauer absorption spectrum of a powder sample shows only single component at RT. The component was described well by Lorentzian. Its isomer shift is 0.023 mm/sec relative to metallic Fe, full width at half maxima (FWHM) of 0.47 mm/sec and no splitting due to quadruple interaction was detected.

Isomer shift of 0.023 mm/sec of $CaFeO_3$ is smaller than the typical value of trivalent iron ion (Fe^{3+}) in the range from 0.45 to 0.55 mm/sec. This suggests the existence of higher valence than trivalent, that can be assigned as tetravalent iron. This value is consistent with the reported one for $SrFeO_3$, for $CaFeO_3$ by Takano *et al.*(1977) and detailed investigation of temperature dependence on $CaFeO_3$ by Nasu *et al.*(1992). Since spectrum at RT is in good agreement to the work by Nasu *et al.* (1992), temperature dependence of Mössbauer spectra of this samples in lower temperature range can be discussed with reference to their work. Narrow FWHM comparable to natural width from metallic iron indicates that the sample was composed of a single phase. This result of the Mössbauer spectrum was concluded that the synthesized sample was the single phase containing tetravalent iron ion.

In addition, the Mössbauer spectrum is very sensitive to the environ-

ment of Fe probe nucleus *i.e.* configuration of oxygen ligands around Fe of $CaFeO_3$. No quadruple splitting in the spectrum indicates the isotropic electric field gradient around Fe and the FeO_6 octahedra with negligible small distortion in $CaFeO_3$.

III–2. Crystal Structural analysis

III–2–1. Structural aspects

The lattice parameters of $CaFeO_3$ have been determined from refined 2θ angles of 25 reflections through conventional least–square procedure. Reflections used for the lattice parameter refinement were selected as to distribute whole reciprocal lattice space to minimize the mechanical error of the diffractometer. The refined lattice parameters are $a = 5.3480(3)$ Å $\approx \sqrt{2}\cdot a_c$ and $c = 7.5730(5)$ Å $\approx 2\cdot a_c$, where a_c is pseudo–cubic subcell parameter. According to the lattice parameters, the unit cell of $CaFeO_3$ contains four formula units.

Laue symmetry of this crystal, which is symmetry of reciprocal lattice, was determined from the statistical distribution of the observed intensity of equivalent reflections. In practice, Laue symmetry has been determined as follows: For the first step, R factors expressed as:

$$R_{refl} = \Sigma(F_i - \bar{F})^2/\Sigma F_i^2, \qquad [3.2.1.1]$$

were calculated for equivalent and for non–equivalent reflections for each possible symmetries. Since the tetragonal symmetrical relation is found from the lattice parameters of this crystal, possible Laue symmetries are limited ones which belong tetragonal system or lower, *e.g.* orthorhombic or mono–

clinic system. Secondly, degree of discrepancy of both R_{refl} factors was checked. Criteria to accept the symmetry is large value of the ratio of R_{refl} factors for crystallographically equivalent reflections to the factor for non-equivalent ones.

Though a real lattice shows tetragonal symmetry, *i.e.* it has 4-fold rotation axis, there is no 4-fold rotation axis in the reciprocal lattice. (This situation occurs in not so many cases, however is not confusing). The most possible Laue symmetry is 2/m in the monoclinic system or mmm in the orthorhombic one. Since there is no prior reason to accept 2/m which belongs to a lower symmetry than orthorhombic, mmm is accepted as Laue symmetry of this crystal.

Systematic absences in reflections were observed at RT in the following series of reflections: h+l=2n+1 in h0l series and k=2n+1 in 0kl series. This indicates a space group D_{2h}^{16}-Pbnm(No.62) in the orthorhombic system on account of Laue symmetry of mmm.

Crystal structure of $CaFeO_3$ at RT is refined with $GdFeO_3$ type structure *i.e.* a "orthorhombic perovskite structure" belonging to the space group Pbnm through full matrix least-squares procedure. As mentioned above there is no prior reason to accept monoclinic 2/m and moreover the systematic absence of reflections seems to support Pbnm even at 113 K. However, Pbnm space group contains only one site for Fe, which cannot describe a structure in the "charge disproportion state". Thus on account of a possibility of an pseudo-high-symmetry due to very weak reflections which break a rule of systematic absence, refinements at 113 K are performed using three space

group candidates: (i) Pbnm with the orthorhombic symmetry which is the same as at RT, (ii) $P2_1/n$ with the monoclinic symmetry and (iii) $P2_1/m$ with the monoclinic symmetry. The two monoclinic space groups belong to sub-groups of the orthorhombic Pbnm. The 3rd candidate of $P2_1/m$ is easily rejected because of no convergence in the refinements. For a structure at 113 K, since the weighted R-factor of 8.20% for $P2_1/n$ is fairly lower than that of 10.9% for Pbnm, a structure based on $P2_1/n$ is concluded to be more reliable. In comparison between the structure at RT and at 113 K, arrangements of Ca and O are quite similar, however, a notable difference is only on Fe site; two kinds of Fe sites are distinguishable clearly at 113 K and make NaCl type arrangement on Fe sub-lattice. As a note, this is the first study for structure of $CaFeO_3$ at low temperature enough to exhibit charge disproportionation of Fe^{4+} into Fe^{3+} and Fe^{5+}. This gives an experimental evidence of "charge disproportionate state" and reveals the arrangement of two different Fe atoms.

Structure of $CaFeO_3$ is shown in Fig. 3.2 schematically; it is applicable at RT and also at 113 K; both Fe(1) and Fe(2) sites are equivalent at RT. Basic feature of this structure is a zig-zag network of FeO_6 polyhedra with almost regular shape shared corners each other which is easy to be derived from the ideal cubic perovskite structure. Fe cation has a site symmetry of $\bar{1}$ in this structure, while it does $\bar{3}m$ in the ideal cubic perovskite structure.

The refined structural parameters at RT and 113 K are listed in Table 3.1(a) and (b) respectively. The observed interatomic distances and bonding angle focused on Fe-O bond are listed in Table 3.2 with data for related

compounds for comparison.

The lattice parameters of a = 5.3480(3) Å and c = 7.5730(5) Å at RT are consistent with those reported by Takeda *et al.* (1978), from powder sample. Crystal structures of $CaFeO_3$ at RT and 113 K are referred to by (**a**+**b**−**b**−) in Glazer's notation. This structure is iso-structure of "natural" perovskite, $CaTiO_3$. Tilting of FeO_6 octahedra in $CaFeO_3$ is due to smaller ionic radii of Ca cation of 1.34Å than that of Sr. The relation between cubic $SrFeO_3$ and tetragonal $CaFeO_3$ is analogous to that between cubic $SrTiO_3$ and orthorhombic $CaTiO_3$.

Interatomic distances of Fe^{4+}–O in $CaFeO_3$ are smaller than that of Fe^{3+}–O in $LaFeO_3$ whose structure is also a orthorhombic perovskite one; this suggests a presence of a higher valence of iron ion than 3+ in $CaFeO_3$. Fe–O distances in $CaFeO_3$ are similar to those of 1.926Å in $SrFeO_{2.9}$ derived from lattice constants obtained using X-ray Debye-Scherrer camera (Oda *et al.* (1977)).

The elongation of FeO_6 octahedron in $CaFeO_6$ observed at RT, however, is quite small (*ca.* 0.4% elongation). A slight elongation is consistent with ^{57}Fe Mössbauer spectra indicating no detectable quadrupole interaction *i.e.* nearly isotropic electric field gradient around Fe. Similar extent of elongation of the FeO_6 octahedron for Fe^{3+} is reported by Marezio, Remeika & Dernier (1970) in $GdFeO_3$ with also orthorhombic perovskite structure. This means the elongation observed in $CaFeO_3$ was not the contribution of the Jahn-Teller distortion which is expected for the high spin configuration of Fe^{4+} in octahedral coordination.

III–2–2. Residual charge density distribution

Residual charge density distribution of $CaFeO_3$ is revealed by difference Fourier map using refined structure factor at RT and 113 K. Note that this is the first observation of the residual electron density in $CaFeO_3$ crystal through single crystal diffractometry. The difference Fourier map at RT and 113 K are shown in Fig. 3.3 for (001) and in Fig. 3.4 for (010) plane respectively. Most remarkable feature of the maps at both temperature is that large residual density peaks are confirmed clearly at the center of Fe^{4+}–O bond. Residual peak maxima at RT is 1.2 e/Å^3 at 0.96 Å from Fe to O. These are contribution of covalent bonding of Fe^{4+}–O. Residual density between Fe and O at 113 K gets larger slightly in comparison to that at RT. Large negative peaks, however, are also observed near positive peaks at 113 K.

IV. Discussion

$CaFeO_3$ and $SrFeO_3$ are oxide systems containing high valence Fe^{4+}. Both oxides show anti-ferromagnetic behavior in their magnetic data. However, a semiconductive behavior of $CaFeO_3$ is very different from the metallic one of $SrFeO_3$. The most remarkable contrast of $CaFeO_3$ to $SrFeO_3$ is illustrated in their Mössbauer spectra at low temperature, which suggests that Fe^{4+} in $CaFeO_3$ exhibits "charge disproportionation" into Fe^{3+} and Fe^{5+} (Takano *et al.* (1977), Nasu *et al.* (1992)), in contrast to that in $SrFeO_3$ which shows no disproportionation (MacChesney *et al.* (1965)).

When Fe cation is octahedrally coordinated by six O anions as is in case of $CaFeO_3$ and $SrFeO_3$, 3d states of Fe cation split into three t_{2g} states and two e_g states due to a ligand field with O_h symmetry on account of *only Fe 3d orbitals*. Fe^{4+} cation has four 3d electrons formally. Two kinds of spin states are possible in $(3d)^4$ electronic configuration depending on a splitting Δ_c between threefold t_{2g} levels and twofold e_g levels: (i) high spin state with $(t_{2g})^3(e_g)^1$ configuration for small Δ_c, (ii) low spin state with $(t_{2g})^4(e_g)^0$ configuration for large Δ_c.

In a system containing FeO_6 octahedra in which Fe^{4+} cation is in high spin state, only one electron in e_g orbital is unstable energetically and expected strong electron-phonon interaction to distort FeO_6 and to lower the symmetry of the ligand field around Fe cation into D_{4h} symmetry. Thus the levels which correspond to e_g levels in O_h environments split into two discrete levels and the lower is occupied to minimize a total energy of the system. Such a distortion is called "Jahn-Teller distortion" and is realized in

$LaMnO_3$ containing Mn^{3+} with a high spin configuration of four 3d electrons. On the other hand, no Jahn–Teller distortion cooperates in case of Fe^{4+} with low spin state because of its stability of $(t_{2g})^4(e_g)^0$ electronic configuration.

The spin state of Fe^{4+} can be considered directly through their magnetic study. In case of $SrFeO_3$, the magnetic moment of Fe^{4+} cannot be provided from the magnetic susceptibility data of stoichiometric $SrFeO_3$, because the data does not obey Curie–Weiss law above T_N. However, a high spin configuration of Fe^{4+} is suggested from an extrapolation of magnetic data on the system $SrFe_{1-x}Co_xO_3$ ($x \geq 0.2$) by Takeda *et al.*(1983). This is also supported through X–ray and ultraviolet photoemission spectroscopic study on stoichiometric $SrFeO_3$ by Bocquet *et al.*(1992).

In case of $CaFeO_3$, a high spin configuration of Fe^{4+} is also suggested from the following arguments:

(1) μ_{eff} of 5.6 μ_B, where μ_B is Bohr magneton, is derived from magnetic data in paramagnetic region above T_N. The value of μ_{eff} is somewhat larger than the spin–only value of 4.9 μ_B for high spin configuration and much larger than 2.8 μ_B for low spin one.

(2) A Mössbauer study under high pressure reveals that a magnetic phase appears above 29 GPa; this magnetic phase is assigned due to a low spin configuration of Fe^{4+}, thus at ambient pressure Fe^{4+} must be a high spin configuration (Nasu *et al.* (1992)).

Note that there exists an argument that a occurrence of "charge disproportionation" into Fe^{3+} and Fe^{5+} requires a high spin configuration of Fe^{4+} before "disproportionate" state. The spin state of Fe^{4+} is concluded to be a high spin

in both $CaFeO_3$ and $SrFeO_3$.

The structural study on $CaFeO_3$ in this thesis reveals:

(1) FeO_6 octahedra share their corners each other, which is similar situation as in the cubic perovskite structure of $SrFeO_3$.

(2) The distortion of FeO_6 is negligibly small and the symmetry of FeO_6 can be considered as O_h symmetry.

(3) The linkage of FeO_6 is a zig–zag style as shown in smaller Fe–O–Fe bond angel than 180° in $SrFeO_3$, which makes structural symmetry down to orthorhombic one or lower.

No or negligibly small Jahn–Teller distortion in $CaFeO_3$ and $SrFeO_3$ seems to be somewhat confusing in spite of a high spin configuration of Fe^{4+} within a classical ligand field theory. (Here is shown an example for the Jahn–Teller effect of high spin Fe^{4+} in the system of $Sr_{0.5}La_{1.5}Li_{0.5}Fe_{0.5}O_4$ with FeO_6 octahedra: Soubeyroux *et al.* (1983) reports two long Fe–O of 2.29 Å and four short ones of 1.79 Å (*ca.* 28% elongation, Table 3.2.) in FeO_6 octahedra and Demazeau *et al.* (1982) reports a large quadrupole splitting of 1.2 mm/sec in its Mössbauer spectrum.)

In this study, the residual electron density is observed clearly at the center Fe^{4+}–O bond in $CaFeO_3$, indicating a formation of a σ–bonding between 2p orbitals of O anion and 3d orbitals of Fe; this is an experimental evidence of a strong covalency of Fe^{4+}–O bond; such a situation, for instance, is illustrated by increase in covalency of Fe–O bond with increase in nominal valence n of Fe^{n+} thorough a theoretical approach by Adachi and Takano (1991) (Fig. 4.1.).

For $SrFeO_3$, the large covalency of Fe^{4+}–O and the straight Fe–O–Fe bonds promote a formation of an anti–bonding σ^* band due to a hybridization between e_g orbitals of Fe and 2p orbitals of O explaining a metallic conductivity. The σ^* band can be assigned to a conduction band near the Fermi level proposed in a band calculation through the self–consistent linear muffin–tin–orbital method by Mathi Jaya *et al.* (1991). The itinerant character of e_g electron is consistent with no Jahn–Teller distortion.

For $CaFeO_3$, on the other hand, a noticeable difference in Fe–O–Fe bond angle is confirmed in comparison to $SrFeO_3$ in this study; the bond angle which is observed to be smaller than 180° weakens a σ–type hybridization between e_g(Fe) and 2p(O). This suppresses a formation of σ^* band; the itinerant character of e_g electron might be lost to some extent. In this case such a breaking of σ^* band is contributed strongly by the bending of Fe–O–Fe bond rather than by a competition of more covalent Ca–O bond than Sr–O; this is supported by little hybridization predicted between orbitals in Ca and those of O (Adachi & Takano (1991)).

At RT, e_g electron of Fe still retains an itinerant character in the same manner as $SrFeO_3$; this is indicated by a relatively high electric conductivity, negligibly small distortion of FeO_6 and a singlet spectrum in Mössbauer spectroscopy. However, with decrease in temperature e_g electron tends to lose a delocalized character suggested by a semiconducting *i.e.* a thermally activated behavior in a temperature dependence of conductivity. As suggested by Mössbauer spectroscopy and confirmed in this diffraction study, at low temperature a lack of electronic delocalization is accompanied by "charge

disproportionation" of Fe^{4+} into two different electronic states of Fe^{3+} and Fe^{5+}, instead of "Jahn–Teller distortion" (Fig. 4.2.). Fe^{3+} with half filled t_{2g} and Fe^{5+} with half filled t_{2g} and e_g orbitals cause no "Jahn–Teller distortion" of FeO_6, which is in accordance with negligibly small distortion of FeO_6 observed at 113 K. $CaFeO_3$ at RT is concluded to be just on a borderline between a metallic region like $SrFeO_3$ and non–metallic charge disproportionate region.

In an octahedral FeO_6 cluster, a covalent mixing between 3d(Fe) and 2p(O) makes bonding and anti–bonding orbitals with e_g and t_{2g} symmetries; both bonding orbitals are mainly contributed by 2p(O) orbitals and both anti–bonding ones have 3d(Fe) parentage; both e_g orbitals are σ–bond type and t_{2g} ones are π–bond type. A calculated level structure for a $(Fe^{4+}O_6)^{8-}$ cluster is derived through the DV–Xα method on account of a self consistent field (Adachi and Takano (1991)), in which the highest occupied level is anti–bonding e_g orbital. The bonding e_g orbitals are filled and anti–bonding one quarter–filled; Adachi and Takano (1991) estimates a 28% contribution of 2p(O) to anti–bonding e_g orbitals in $(Fe^{4+}O_6)^{8-}$ cluster. A superposition of these bonding and anti–bonding σ–bonds is the origin of the residual electron density at the middle of Fe^{4+}–O bond revealed in difference Fourier map. A residual electron density still retains on the Fe–O bond similarly as at RT even at 113 K in the charge disproportionate state. An origin of this is explained as follows:

(1) for Fe^{3+}, there is a superposition of fully filled bonding σ bonds and half–filled anti–bonding ones.

(2) for Fe^{5+}, there are only fully filled bonding σ bonds, but they have a large contribution of 3d(Fe) by 38% (Adachi and Takano (1991)) due to stronger covalency than that of Fe^{4+}–O bond.

It is important to note that in $CaFeO_3$ the charge disproportionate phase does not require any superstructures of the structure at RT, in other words the structural periodicity is held during the change into the disproportionate phase.

References

Adachi, H. & Takano, M. (1991). *J. Solid State Chem.* **93**, 556–66.

Ballhausen, C. J. (1962): *"Introduction to Ligand–Field–Theory"*, McGraw–Hill, New York.

Bednorz, J. G. & Müller, K. A. (1986). *Z. Phys.* **B46**, 189–93

Bishop, D. M. (1973): *"Group Theory and Chemistry"*, Dover, New York.

Bocquet, A. E., Fujimori, A., Mizokawa, T., Saitoh, T., Namatame, H., Suga, S., Kimizuka, N., Takeda, Y. & Takano, M. (1992). *Phys. Rev. B* **45**, 1561–70.

Demazeau, G., Buffat, B., Pouchard, M. & Hagenmuller, P. (1984). *J. Solid State Chemistry.* **54**, 389–99.

Glazer, A. M. (1972). *Acta Crystallogr.* **B28**, 3384–92.

Glazer, A. M. (1975). *Acta Crystallogr.* **B31**, 756–62.

Gray, H. B. (1965): *"Electrons and Chemical Bonding"*, Benjamin, New York.

Grenier, J. C., Schiffmacher, G., Caro, P., Pouchard, M. & Hagenmuller, P. (1977). *J. Solid State Chem.* **20**, 365–79.

Kamimura, H., Sugano, S., Tanabe, Y. (1969): *"Ligand Field Theory and Its Applications"*, Syokabo, Tokyo. (in Japanese).

MacChesney, J. B., Sherwood, R. C. & Potter, J. F. (1965). *J. Chem. Phys.* **43**, 1907.

Marezio, M., Remeika, J.P. & Dernier, P.D. (1970). *Acta Crystallogr.* **B26**, 2008–22.

Mathi Jaya, S., Jagadish, R., Rao, R. S. & Asokamani, R. (1991). *Phys. Rev. B* **43**, 13274–9.

Nagata, M. & Kanno, R. (1994). personal communication.

Nasu, S., Abe, T., Yamamoto, K., Endo, S., Takano, M. & Takeda, Y. (1992). *Hyperfine Interaction* **70**, 1063–6.

Oda, H., Yamaguchi, Y., Takei, H. & Watanabe, H. (1977). *J. Phys. Soc. Japan.* **42**, 101–6.

Sasaki, S. (1987). *KEK Internal Report* **87–3**. (unpublished)

Sasaki, S., Prewitt, C. T., & Liebermann, R. C. (1983). *Am. Mineral.* **68**, 1189–98.

Sasaki, S., Prewitt, C. T. & Bass, J. D. (1987). *Acta Crystallogr.* **C43**, 1668–74.
Shannon, R. D. (1976). *Acta Crystallogr.* **A32**, 751.

Sleight, A. W., Gillson, J. L. & Bierstedt, P. E. (1975). *Solid State Commun.* **17**, 27.

Soubeyroux, J. L., Buffat, B., Chevreau, N. & Demazeau, G. (1971).*Physica B* **120**, 227.

Takano, M., Nakanishi, N., Takeda, Y., Naka, S. & Takeda, T. (1977). *Mater. Res. Bull.* **12**, 923.

Takeda, T., Komura, S. & Fujii, H. (1983). *J. Magn. Magn. Mater.* **31–34**, 797.

Takeda, Y., Naka, S., Takano, M., Shinjo, T., Takeda, T. & Shimada, M. (1978). *Mater. Res. Bull.* **13**, 61.

Tsuda, N., Nasu, K., Fujimori, A. & Siratori, K. (1993): *"Electronic Conduction in Oxides (2nd Ed.)"*, Syokabo, Tokyo. (in Japanese).

Tsuda, N., Nasu, K., Yanase, A. & Siratori, K. (1991): *"Electronic Conduction in Oxides"*, Spring–Verlag, Berlin.

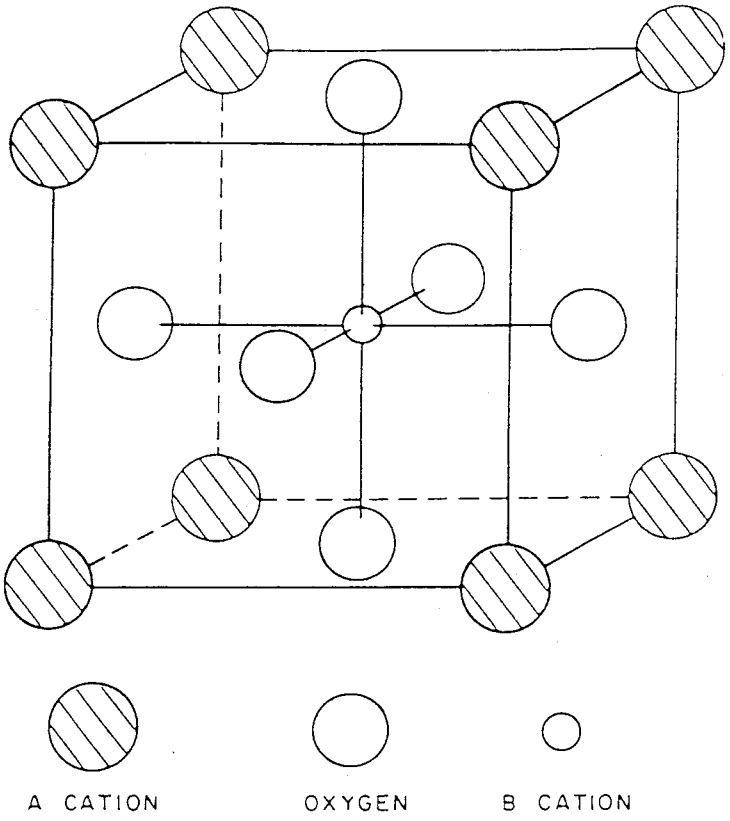

Fig. 1.1. Perovskite structure

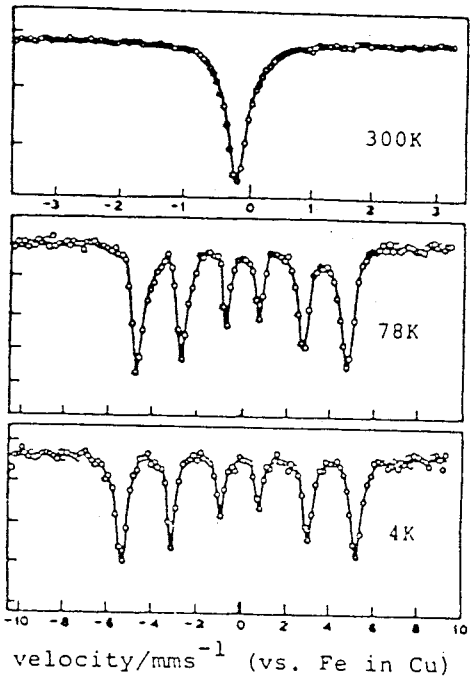

(a)

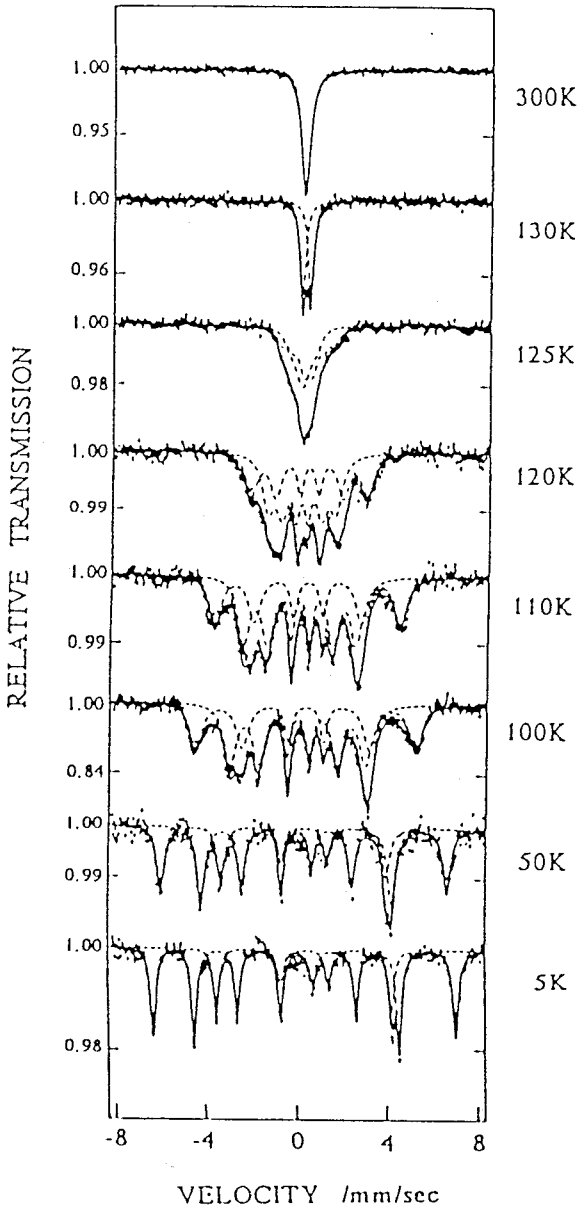

(b)

Fig. 1.2. Mössbauer spectrum at various temperature for (a) $SrFeO_3$, after MacChesney, and (b) $CaFeO_3$, after Nasu *et al.*

$$Ca_2Fe_2O_5 + \frac{1}{2}O_2 \longrightarrow 2CaFeO_3$$

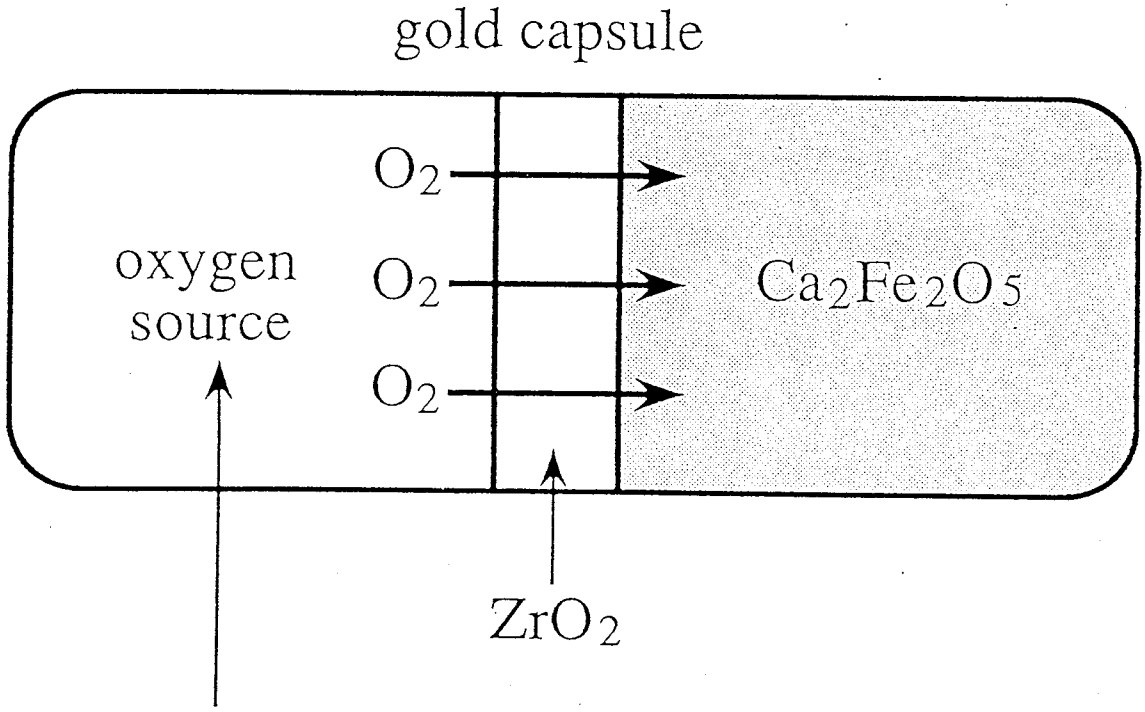

$$KClO_4 \longrightarrow KCl + 2O_2$$

$$2CrO_3 \longrightarrow Cr_2O_3 + \frac{3}{2}O_2$$

$$KIO_4 \longrightarrow KIO_3 + \frac{1}{2}O_2$$

$$CaO_2 \longrightarrow CaO + \frac{1}{2}O_2$$

thermal decomposition

Fig. 2.1. Sample synthesis under high oxygen partial pressure

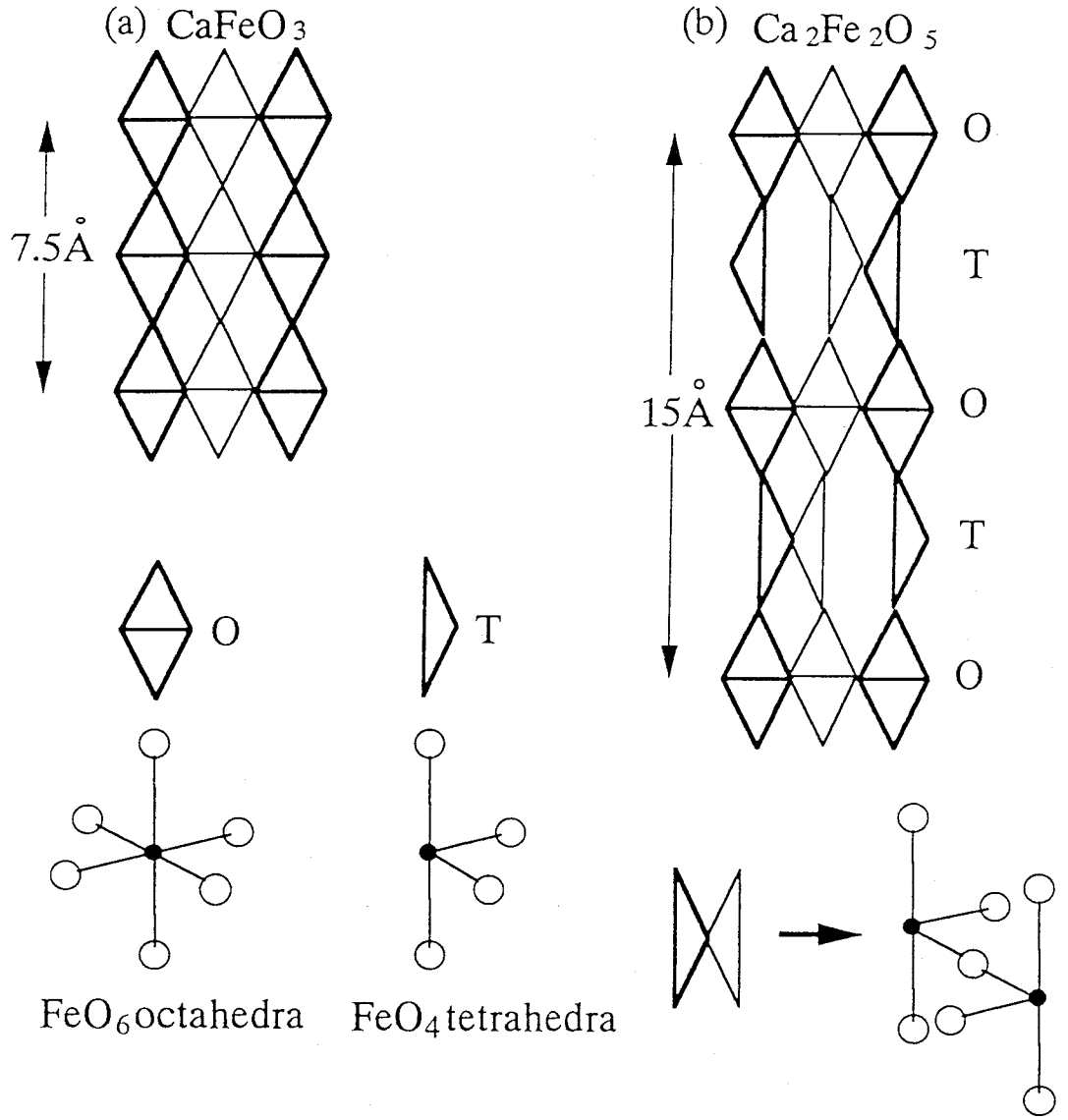

Fig. 2.2. Brownmillerite structure (b) as oxygen defective perovskite in comparison to perovskite structure (a)

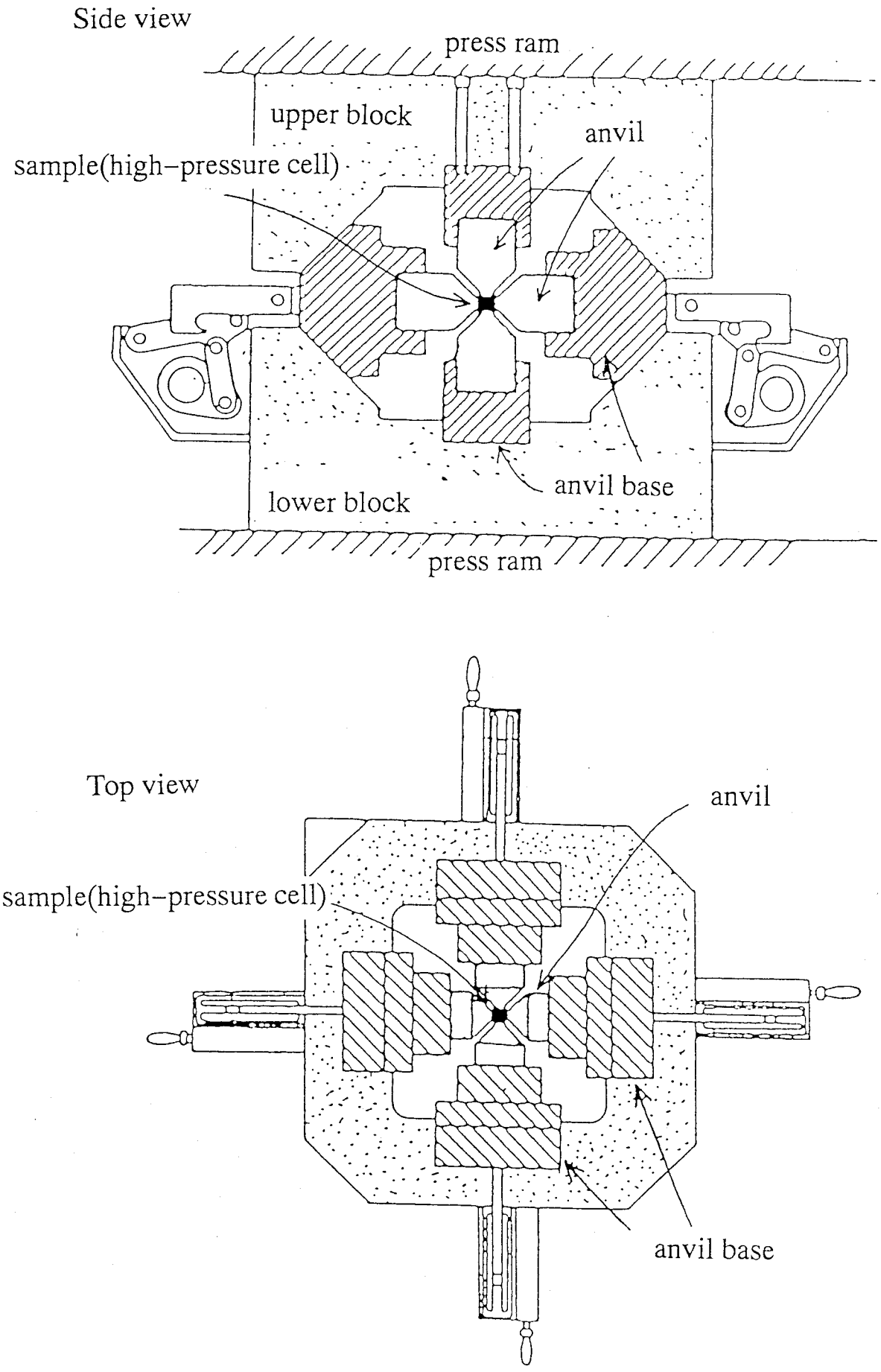

Fig. 2.3.(a). Cubic anvil type apparatus

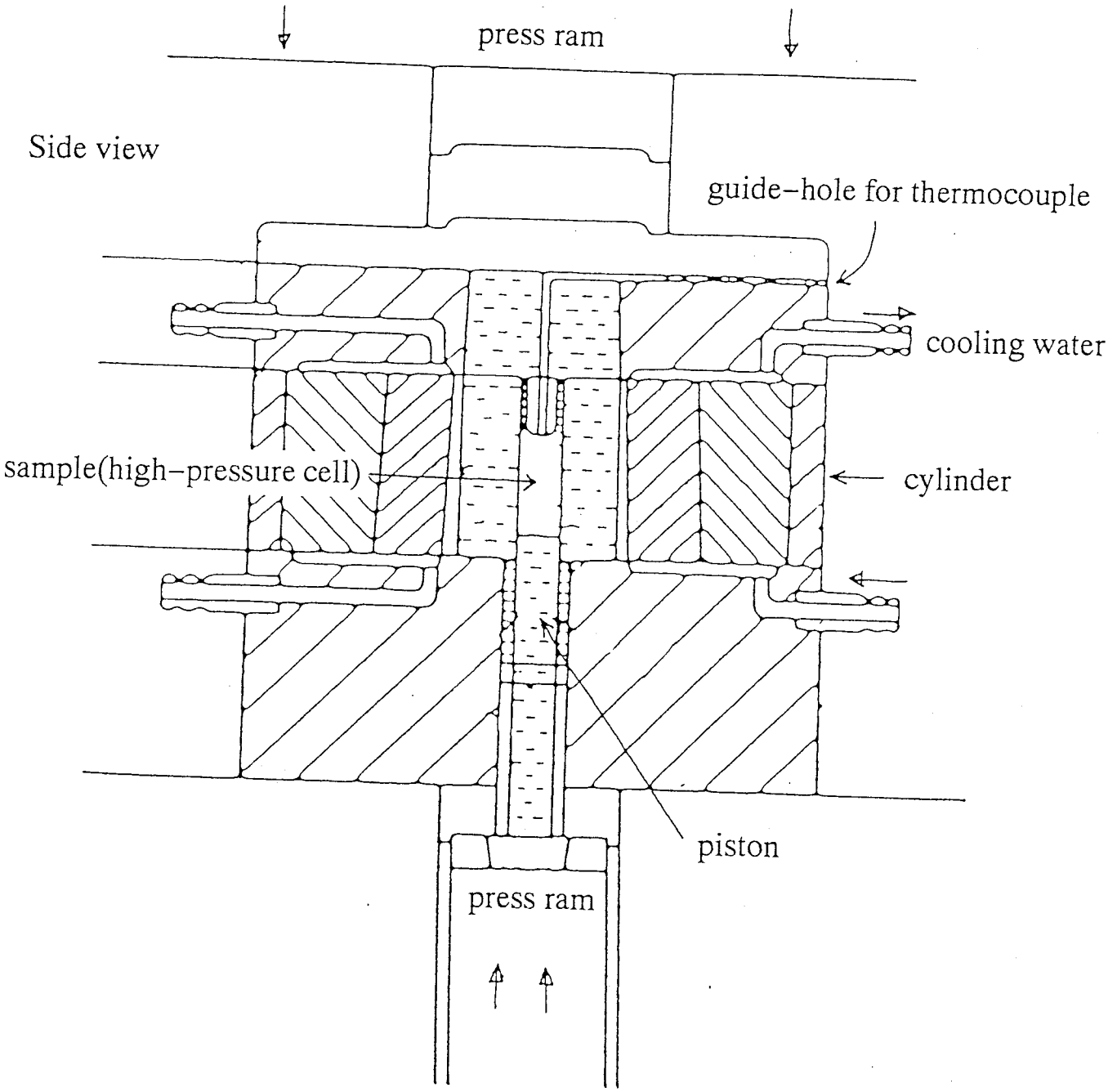

Fig. 2.3.(b). Piston cylindrical device

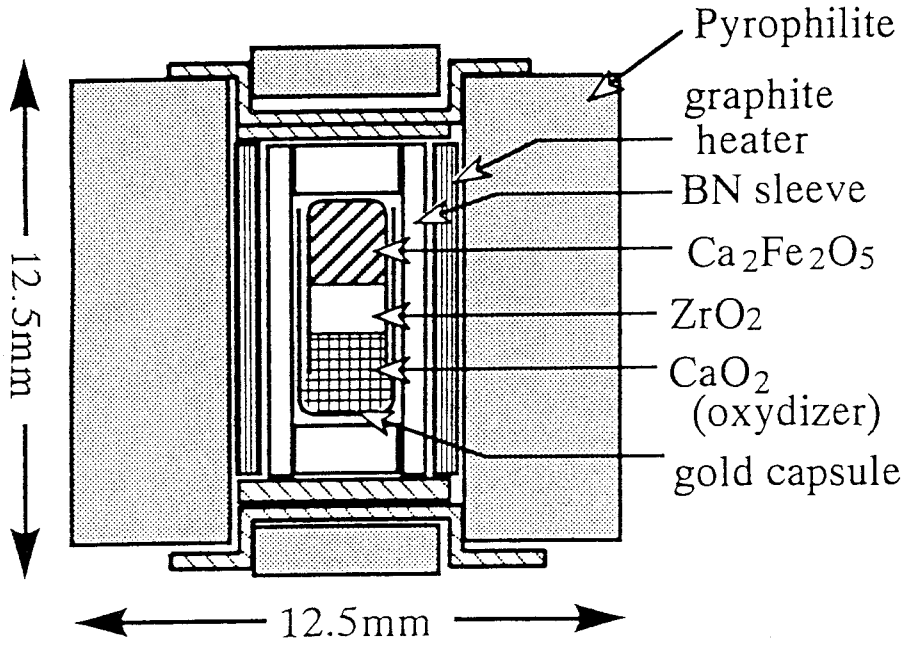

Fig. 2.4.(a). Cell assemblage for the cubic anvil type apparatus

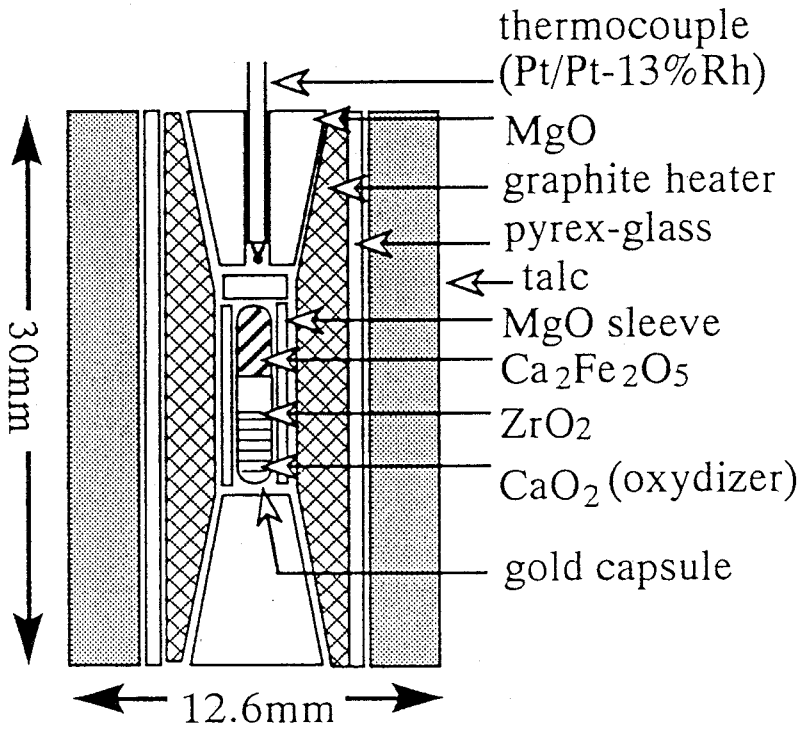

Fig. 2.4.(b). Cell assemblage for the piston cylindrical device

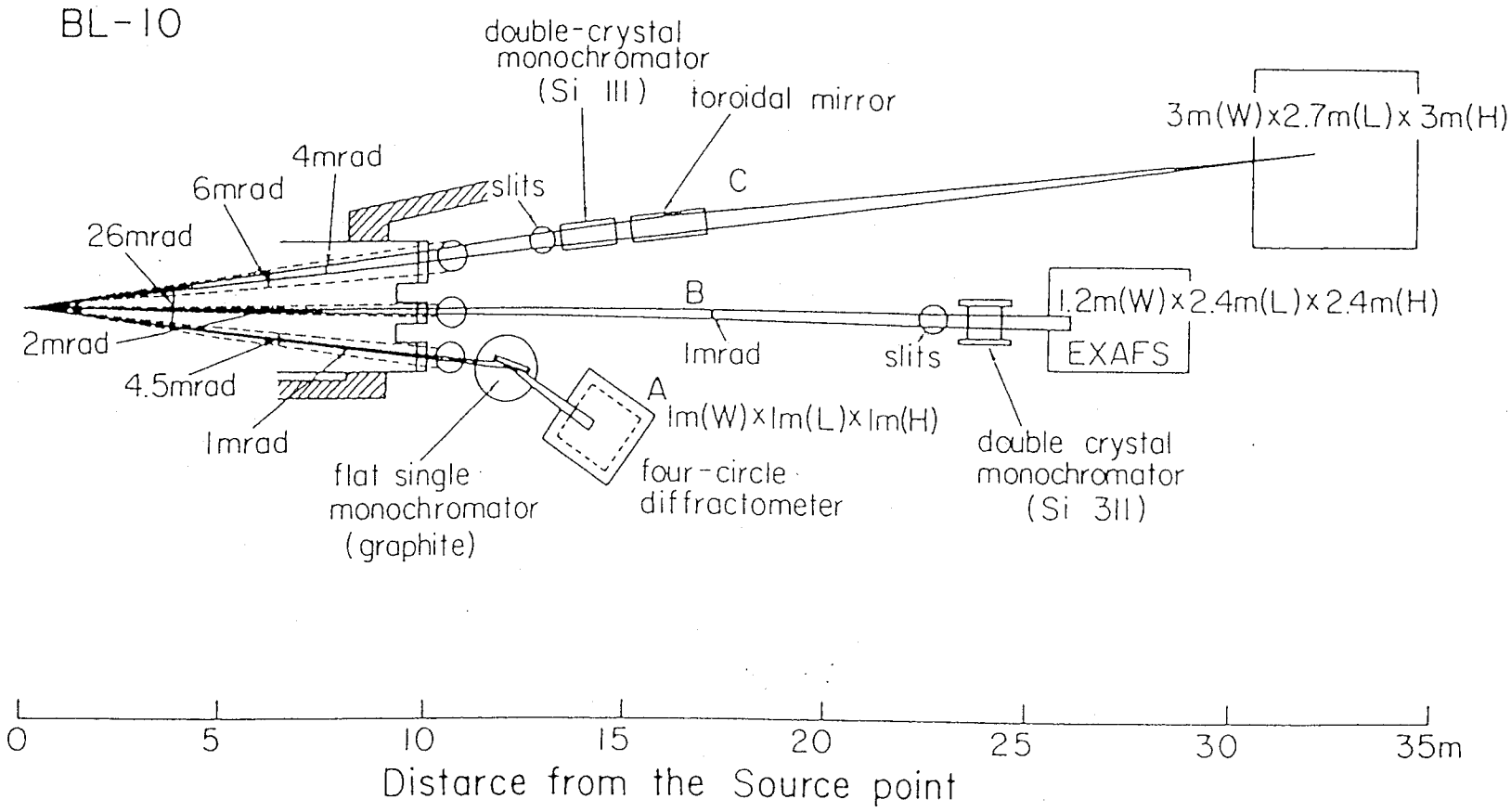

Fig. 2.5. Arrangement of beam line 10 (BL–10)

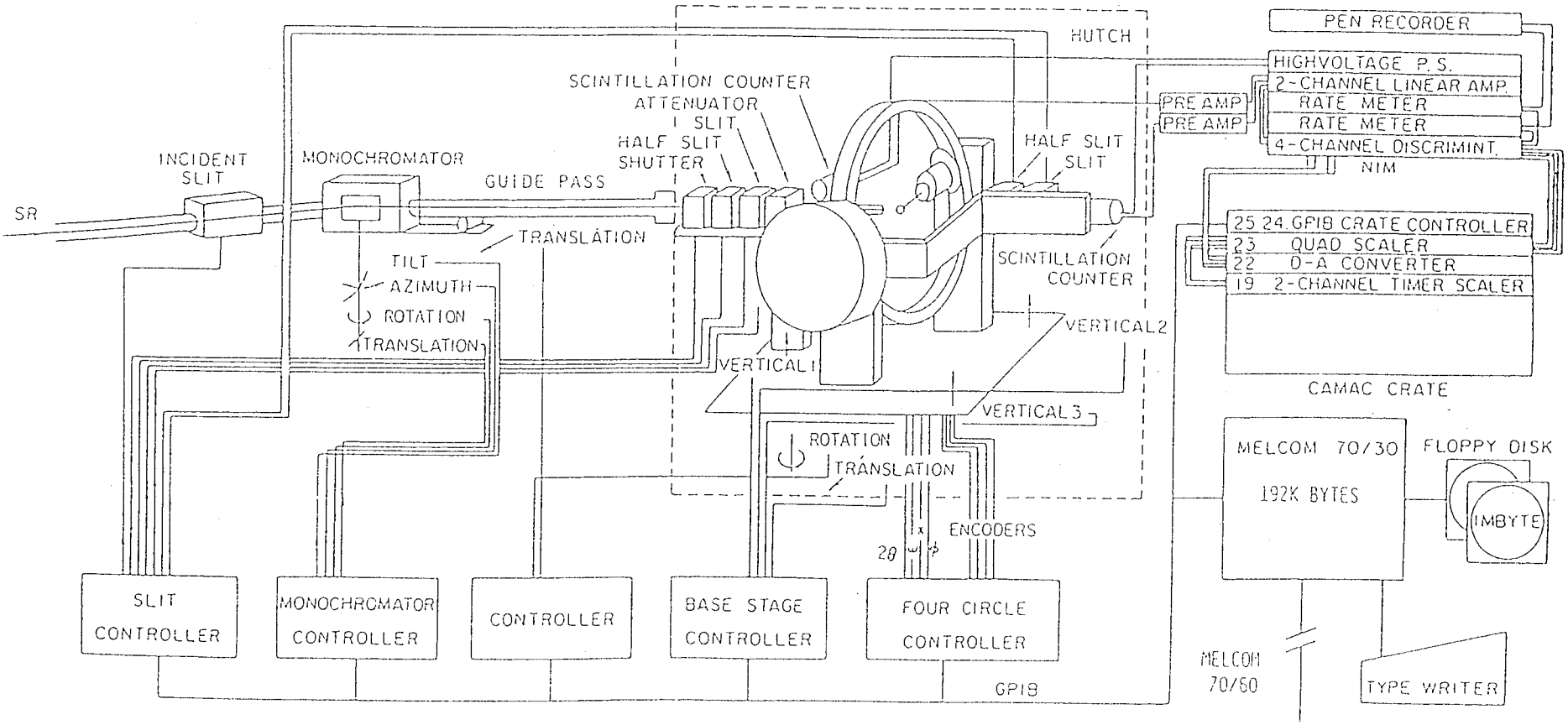

Fig. 2.6. Diagram for the vertical four-circle diffractometer at BL-10A

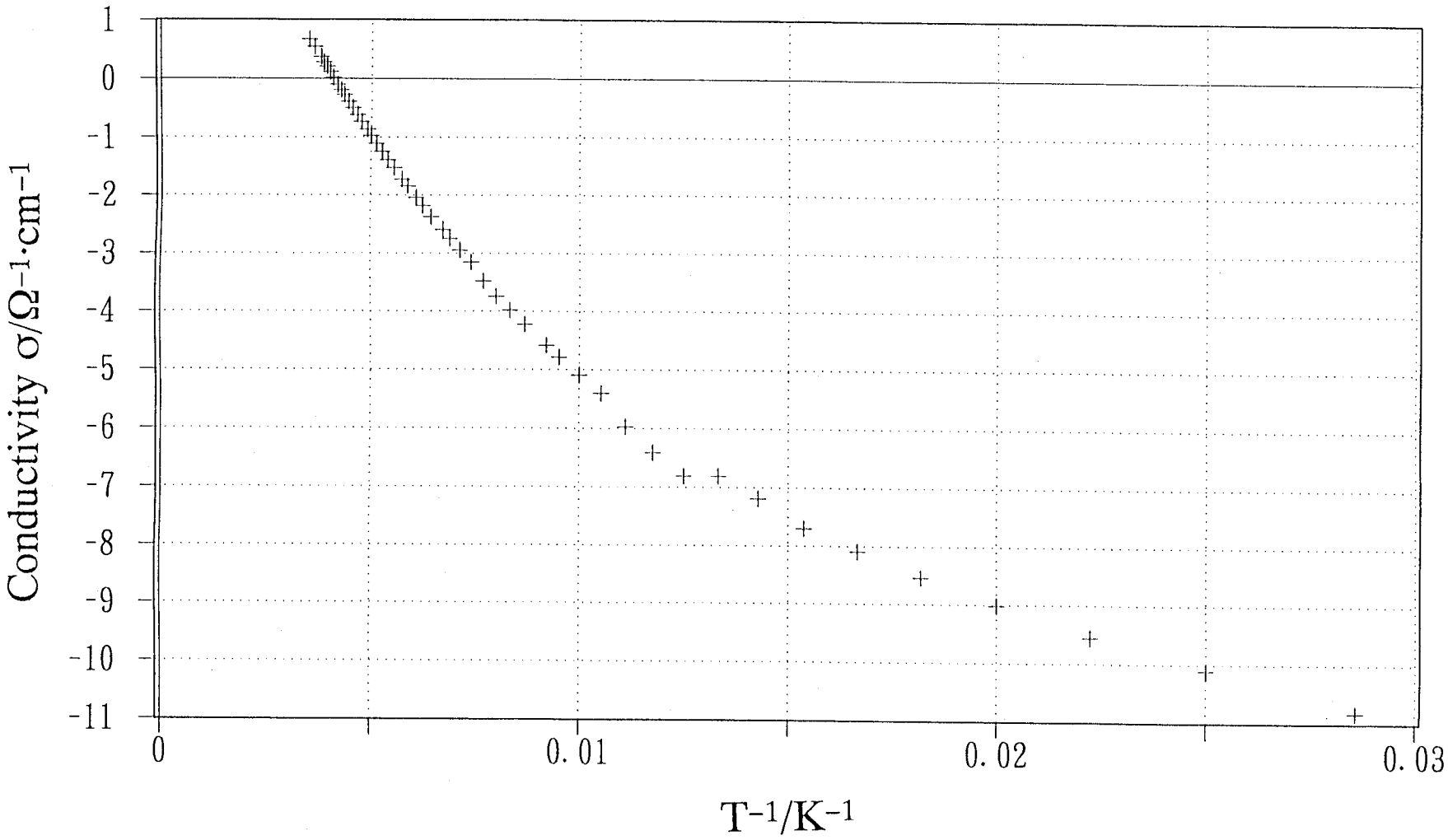

Fig. 3.1. Conductivity versus reciprocal temperature of $CaFeO_3$

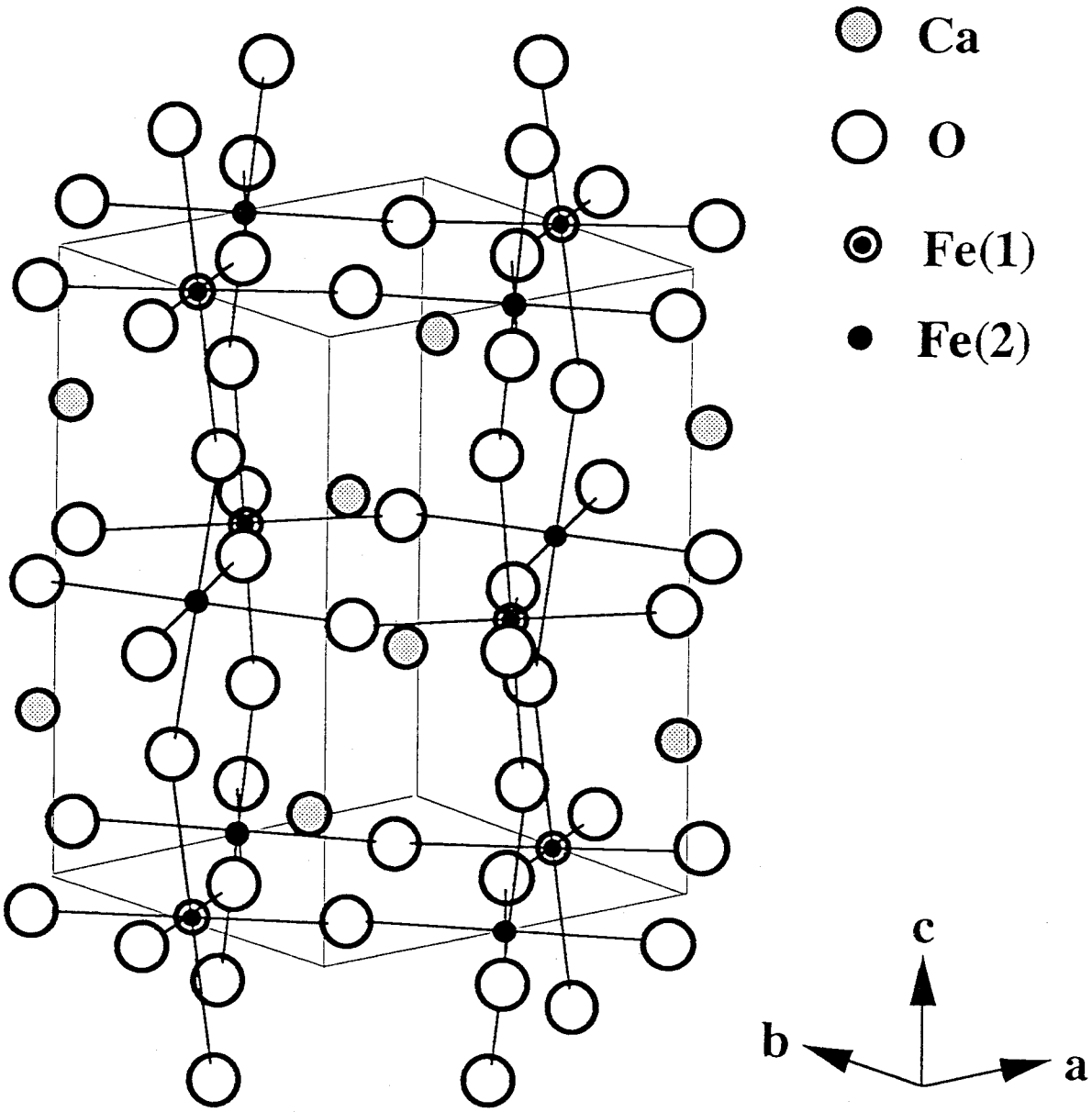

Fig. 3.2. Crystal structure of $CaFeO_3$ at RT and 113 K
note that Fe(1) and Fe(2) are equivalent positions at RT

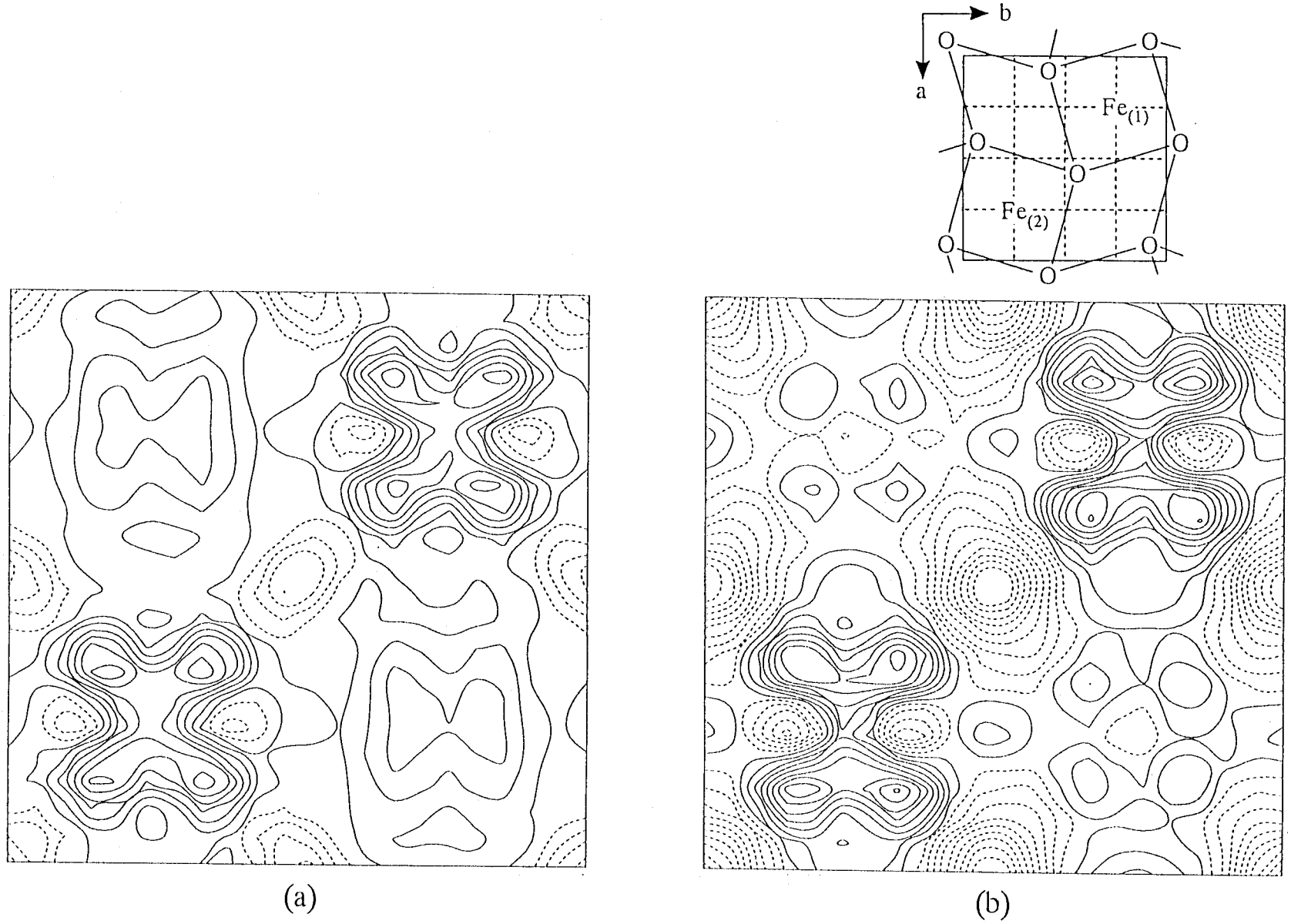

Fig. 3.3. Difference Fourier maps of $CaFeO_3$ for (001) plane at (a) RT and (b) 113 K contour intervals of 0.2 e/Å^3 with dashed line for negative contour

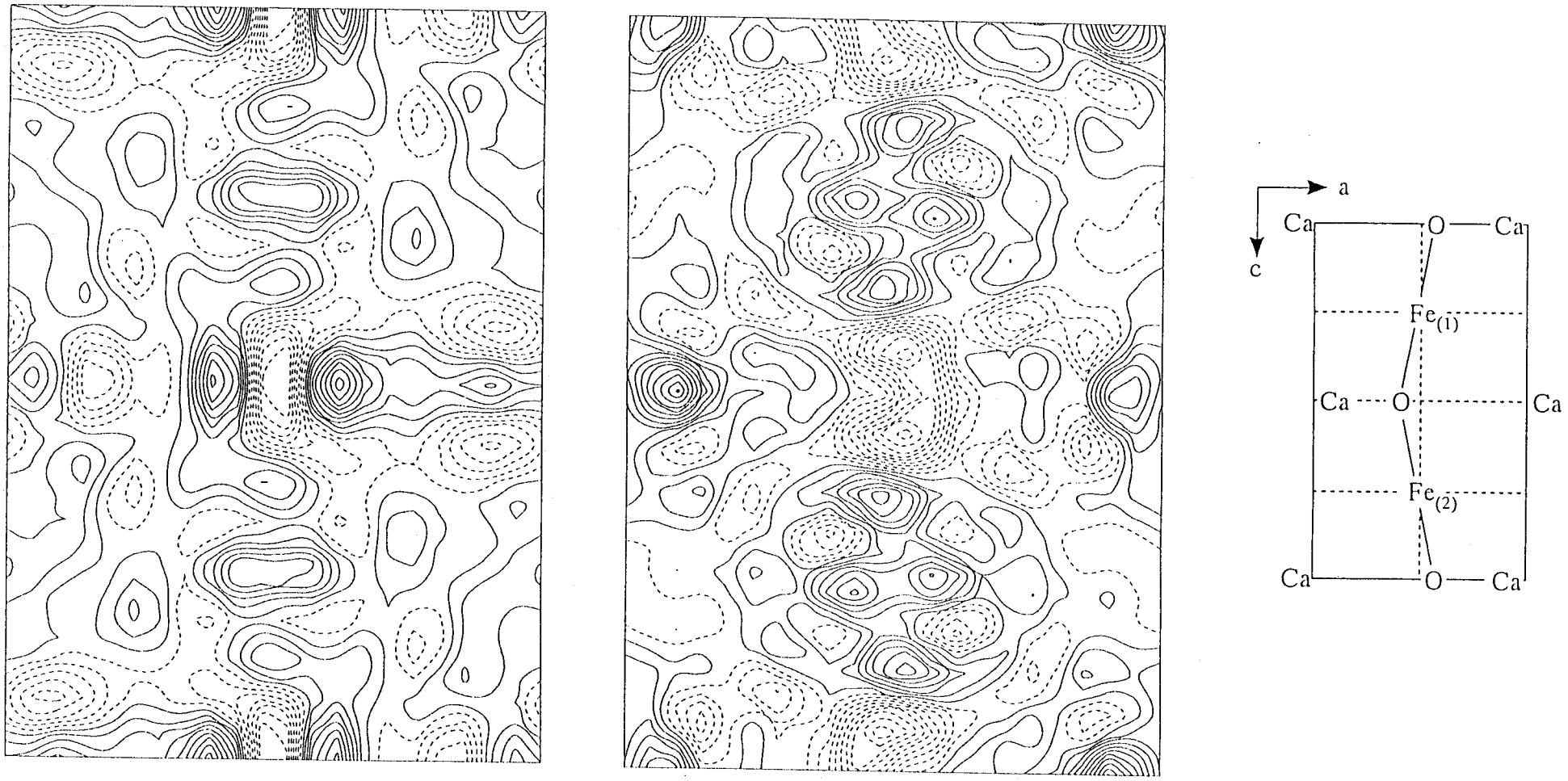

Fig. 3.4. Difference Fourier maps of $CaFeO_3$ for (010) plane at (a) RT and (b) 113 K contour intervals of 0.2 e/Å^3 with dashed line for negative contour

Table 3.1.(a). Refined structural parameters of $CaFeO_3$ at RT

Pbnm, Z = 4, a = 5.3480(3), b = a*, c = 7.5730(5) Å
R(F) = 0.0735, wR(F) = 0.1222

	x	y	z	B
Ca	−0.004(1)	−0.004(1)	0.25	1.92(10)
Fe	0.0	0.5	0.0	0.60(7)
O(1)	0.035(4)	0.542(4)	0.25	1.5(3)
O(2)	0.281(3)	−0.282(3)	−0.031(2)	1.3(3)

* coincidence within experimental error

Table 3.1.(b). Refined structural parameters of $CaFeO_3$ at 113K

Refined Model(1)

Pbnm, Z = 4, a = 5.3409(3), b = a*, c = 7.5585(13) Å
R(F) = 0.0678, wR(F) = 0.1093

	x	y	z	B
Ca	−0.004(2)	−0.011(1)	0.25	1.74(9)
Fe	0.0	0.5	0.0	0.50(7)
O(1)	0.043(4)	0.543(5)	0.25	1.9(4)
O(2)	0.282(3)	−0.287(3)	−0.031(2)	1.3(3)

Refined Model(2)

$P2_1/n$, Z = 4, a = 5.3409(3), b = a*, c = 7.5585(13) Å, β = 90°*
R(F)=0.0616, wR(F)=0.0820

	x	y	z	B
Ca	0.0022(8)	−0.0121(3)	0.2449(5)	1.72(3)
Fe(1)	0.0	0.5	0.0	0.64(3)
Fe(2)	0.0	0.5	0.5	0.36(3)
O(1)	0.043(4)	0.543(5)	0.25	2.6(2)
O(2)	0.282(3)	−0.287(3)	−0.031(2)	1.6(3)

* coincidence within experimental error

Table 3.2. Interatomic distances and bonding angles of $CaFeO_3$ focused on Fe–O bond, including data for related compounds

	Fe–O distances / Å	
$SrFeO_3$	1.925 x 6	Takeda *et al.*
$Sr_{0.5}La_{1.5}Li_{0.5}Fe_{0.5}O_4$	1.88 x 4 2.36 x 2	Soubeyroux *et al.*
$CaFeO_3$ (298 K)	1.920(2) x 2 1.919(8) x 2 1.926(8) x 2	This work
$CaFeO_3$ (113 K)	1.915(2) x 2 1.911(12) x 2 1.913(14) x 2 1.915(2) x 2 1.911(12) x 2 1.913(14) x 2	This work
	Fe–O–Fe angles / deg.	
$Sr_2LaFe_3O_{8.94}$	173.8	Battel *et al.*
$CaFeO_3$ (298 K)	160.8(7) 159.2(4)	This work
$CaFeO_3$ (113 K)	161.5(6) 161.9(8) 161.9(8)	

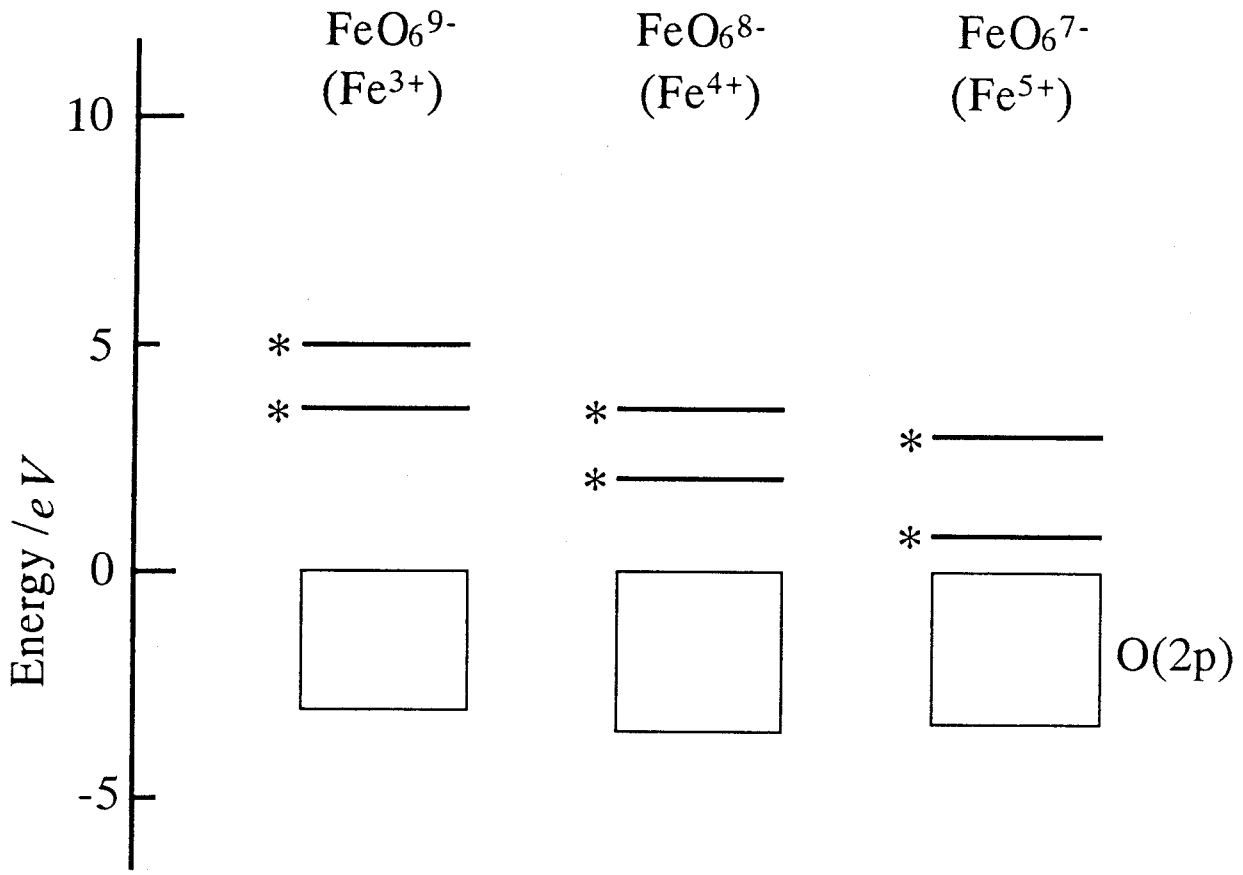

Fig. 4.1. Level structures for $(Fe^{n+}O_6)^{(12-n)-}$ cluster, after Adachi & Takano, * indicates levels mainly contributied by 3d(Fe)

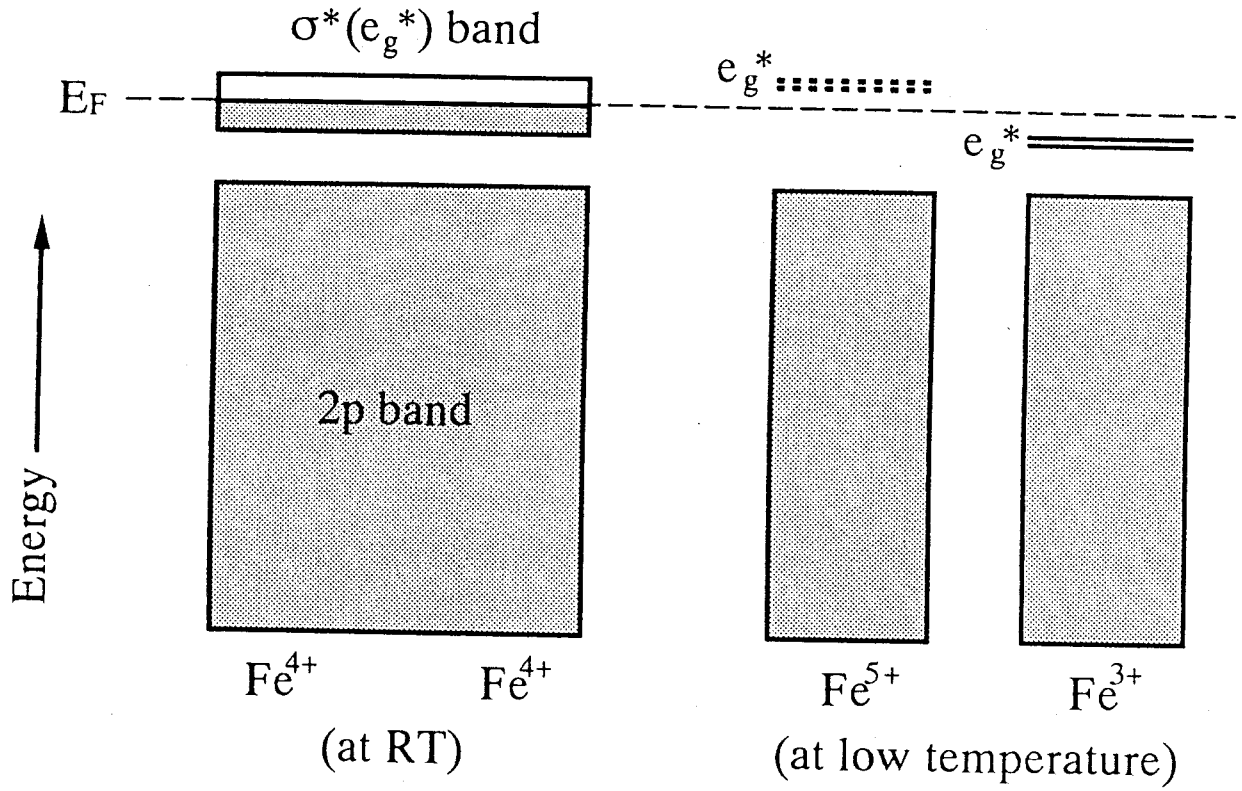

Fig. 4.2. Schematic level structures for $CaFeO_3$ at RT and at low temperature (in charge disproportionation state)

Chapter 3. APPLICATION to ^{13}C DIAMOND

I. Introduction

I–1. Some physical properties

Diamond is a crystalline form of carbon (C) and a typical example of the compound with *covalent bonding*; it is known as one of the hardest substance and the best thermal conductor, which attracts much attention for industrial use. Its hardness and the high thermal conductivity might be easily understand due to its strong covalent bonding.

The crystal structure is referred as the "diamond structure"; its space group is $Fd3m(O_h^7)$ with fcc lattice; all C atoms sited at 8a position with $\bar{4}3m$ symmetry, which is of a lower symmetry than the point group of the diamond crystal structure of m3m; the center of symmetry of this structure is not found *at* 8a sites but *at the middle of* 8a sites (Fig 1.1).

In recent decades, development in synthesis techniques of diamond can provide samples with various isotope concentration (Strong & Wentorf (1991); Banholzer & Anthony (1992); Angus & Hayman (1988)); many studies on diamond have been concerned with isotope effects of ^{13}C concentration on physical properties through both experimental and theoretical approaches: thermal conductivity (Anthony *et al.* (1990)), elastic moduli (Ramdas *et al.* (1993)), Raman spectrum (Nishida (1992), Hass *et al.* (1992)), vibrational, vibronic absorption (Collins *et al.* (1988)), indirect gap (Collins *et al.* (1990)), and lattice constants (Banholzer *et al.* (1991)).

Banholzer *et al.* (1991) reported the lattice constant of natural and ^{13}C diamond by X–ray diffraction using the powder samples and single–crystals. Holloway *et al.* (1991 & 1992) examined the influence of the isotope ratio on

the lattice constant of mixed crystals of $^{13}C_x{}^{12}C_{(1-x)}$ by single-crystal X-ray diffractometry. They made the precise measurements of the 400 Bragg peak positions using CuKα_1 radiation from Si (111) double-crystals monochromator, and reported the lattice constant decreasing linearly with ^{13}C content according to the expression

$$a(X) = 3.56714 - 5.4 \times 10^{-4}X, \qquad [1.1.1]$$

the fractional difference $\Delta a/a$ between both end-compositions being -1.5×10^{-4}.

Collins *et al.* (1988) estimated the fractional volume difference between natural diamond and ^{13}C diamond as $\Delta V/V = -6.38 \times 10^{-4}$ from London theory (London (1958)) in their vibrational and vibronic absorption study. [Note that the difference in the unit-cell volumes of crystals composed of single element having various isotope ratios was discussed from thermodynamical considerations by London (1958). It has been reported that the fractional volume $\Delta V/V$ of the following isotope pairs is correlated with their fractional mass ratio $\Delta M/M$; ^3He and ^4He (Wilkis (1967)), ^{20}Ne and ^{22}Ne (Bolz & Maner (1962)), ^{74}Ge and $^{72.6}Ge$ (Buschert *et al.* (1988)), ^7Li and ^6Li (Coington & Montgomery (1957)), ^{64}Ni and ^{58}Ni (Kogan & Bulatov (1962)) and oxides systems containing, ^{24}Mg and ^{26}Mg, ^{40}Ca and ^{48}Ca, ^{58}Ni and ^{64}Ni (Berezin & Ibrahim (1988)).]

In addition, one of the recent and most attractive topics is the 50 % increase in the thermal conductivity of single crystal sample of almost pure ^{12}C at room temperature in comparison with a sample of natural isotope abundance *i.e.* of 1.1 % ^{13}C, which is reported by Anthony *et al.* (1992) and

confirmed by Onn *et al.* (1992) and Olson *at al.* (1993). This enhancement of thermal conductivity is larger than that expected from a decrease of phonon scattering by ^{13}C isotopes alone.

I–2. Charge density studies on covalent diamond

Diamond has strong covalent bonding; the covalent bonding of C atoms causes a localized charge density between C–C bonding. The simplicity of its structure and high symmetry of atom positions have been leading much interest on the charge density distribution in diamond crystal.

Brill *et al.* (1939) firstly examined the electron distribution of a covalent bonding in comparison with the that of the ionic bonding in NaCl through X–ray diffraction. Göttlicher & Wölfel (1959) obtained data set with more accuracy and of absolute scale using a powder sample; this set of observed structure factors has been analyzed for charge density studies by many authors: Weiss (1964); Dawson (1967 & 1975); Dawson & Sanger (1967); Kurki–Suonio & Ruuskanen (1971); McConnell & Sanger (1970); Stewart (1973); Price & Maslen (1978). The data of the "forbidden" 222 reflection is usually combined, which is measured by Renninger (1955) or Weiss & Middleton (1965).

Many approaches also has been improved on non–spherical charge density around the atoms and the Debye–Waller factor due to thermal vibrations of the atoms in natural diamond; applying Hartree–Fock calculation performed by McConnel & Sanger (1970); a generalized X–ray scattering factor proposed by Stewart (1973); a deformation–density model of multi–

pole terms of exponential form by Price & Maslen (1978); a pseudo-potential density-functional method by Denteneer and van Haeringen (1985).

The absolute measurement of structure factor has been developed recently for diamond-like crystal through the Pendellösung beats of thin single crystal wafers sample by Takama & Sato (1988), and Deutsch & Hart (1985).Takama *et al.* (1990) provides the absolutely scaled set of structure factors of diamond by the Pendellösung beat method. This set of structure factors has stimulated the charge density studies in attempt comparing experiment and theory; this set is analyzed through many methods and has demonstrated its agreement to many sets of theoretical structure factors by Spackman (1990).

In addition, the weak "forbidden" reflection of 222, which is clear evidence of a deformation of charge density from sphere distribution, is obtainable more precisely by the recent progress in a strong X-ray source from synchrotron orbital radiation; the origin of such reflection is also of interest (Tischler & Batterman (1984); Kotani & Yamanaka (1991))

I-3. Purpose

As mentioned above, the influence of isotope composition in the crystalline materials has been extensively studied from both theoretical and experimental points of view. The recent enhancement of the thermal conductivity of diamond has been shown to be strikingly sensitive to the ^{13}C isotope concentration. Isotope effects on physical properties of materials are directly due to a change in lattice vibration *i.e.* phonons.

In a crystallographic study anharmonic thermal motion of atoms in a crystal is applicable using an accurate set of structure factors. (The method considering an anharmonic motion of an atom will be described in Experimental section.) The purpose of this study is focused on the ^{13}C isotope influences on anharmonic thermal vibration of atoms in diamond, which atoms are not found at the center of symmetry; charge density deformation mainly due to the covalent bonding is to be treated near around atoms; bonding feature will be demonstrated after the treatment of thermal motion of and charge distribution around atoms; these approaches are to be performed by the help of X-ray diffraction technique using the synchrotron radiation source with great advantage.

II. Experimental

II–1. Sample preparation

Single–crystals of diamond with various isotope ratios between ^{13}C and ^{12}C have been synthesized using flat–belt type high pressure apparatus (Kanda *et al.* (1989)). The isotope ratios of the grown diamond specimens as well as natural diamond were determined by the secondary ion mass spectrometer (HITACHI–IMA2A SIMS). The isotope contents were measured using O^{+2} primary ion beam on the crystal surface, where samples were held on Pt plate to keep high electric conductivity around the samples because diamond is a good insulator, of 100 μm across for sputtering time of 1 hour. The isotope ratio represents the mean value of more than five observed data. The observed ratios $[^{13}C]/([^{12}C]+[^{13}C])$ in the natural and four synthesized diamonds were proved to be 2.0 ± 0.8, 18.3 ± 1.1, 48.1 ± 1.0, 67.3 ± 1.1 and 98.5 ± 0.4 wt%. The crystals with an octahedral shape which is roughly approximated to a sphere of *ca.* 20 μm in radius were selected for the single–crystal diffraction studies.

II–2. Dependence of lattice constant on ^{13}C isotope contents

A very precise measurement of the d–spacing is required in order to investigate the influence of the isotope ratio on the diamond lattice constant. The Bragg angle θ observed in a normal single–crystal diffraction experiments has to consider the following error $\delta\theta$:

$$\delta\theta = \delta\theta_1 + \delta\theta_2 + \delta\theta_3 + \delta\theta_4, \qquad [2.2.1]$$

where $\delta\theta_1$ comes out from mismatching θ, ω, χ, and ϕ–axis of four–circle

diffractometer, $\delta\theta_2$ from the divergence of the incident beam, $\delta\theta_3$ from the broadness of energy distribution of the radiation expressed by $\Delta E/E$, and $\delta\theta_4$ from the scattering of the diffraction beam. $\delta\theta_1$ depends on mechanical adjusting of the center of four-circle diffractometer. The Bragg angle was measured by means of Bond method $\theta = \pm 90° + (\theta_1 + \theta_2)/2$ (Bond (1960)). This method of determining θ eliminates the zero error. The positron synchrotron radiation source at Photon Factory, which radiation was emitted from normal bending magnet with the maximum energy of 2.5 GeV and the maximum ring current of 300 mA. The radiation provides an extremely collimated beam and lessened the error of $\delta\theta_2$.

A monochromated beam of wave length $\lambda = 0.697148 \pm 2.8 \times 10^{-5}$ Å was obtained from a flat-plate Si (111) crystal, which had an energy resolution of $\Delta E/E = 4 \times 10^{-5}$. The length was confirmed with NBS Si standard reference material 640b having a lattice constant of $a = 5.430940 \pm 3.0 \times 10^{-5}$ Å. $\delta\theta_4$ was reduced by the narrow scattering slit of 0.3°.

The measurement was made on four-circle diffractometer equipped with an encoder having an accuracy of 0.001°. Details of the diffractometer are described by Sasaki (1989) and Sakamaki *et al.* (1984).

The present determination of the lattice constant was performed by taking an average of the θ values obtained from 25 independent measurements for three sets of high angle reflections, {531}, {620} and {642}.

Diffraction intensities were measured by the ω-2θ step scanning mode with a increment step of 0.01° in 2θ and a counting time of 1 sec. per step. The profile fitting was applied to the step-counted intensities by the pseudo-

Voigt function (Young & Wiles (1982)):

$$P(2\theta_i) = c[\eta \exp(2\theta_i/\Gamma)^2 + (1-\eta)[1+4B(2\theta_i/\Gamma)^2], \qquad [2.2.2]$$

and provided an accurate intensity together with peak position, full width at half maximum (Γ) and a fraction of Gaussian components (η parameter). The peak position of each reflection was determined with a precision of 9 sec, and the FWHM of most of the reflections was about 200 arc sec.

The temperature in the hutch of the experimental station was controlled at 299 ± 0.5 K, to minimize errors due to thermal expansion. The precision of the lattice constants measurement was in the order of 10^{-5} Å.

II–3. Crystal structure analysis

II–3–1. Data collection procedure

The diffraction intensities were measured for two end–components of the series of isotope solid solution *i.e.* natural (2.0 wt%) and ^{13}C (98.5 wt%) diamond by the ω–2θ step scanning mode with an increment of 0.01° in 2θ and scanning speed of 1 sec. per step. Diffraction intensities of reflections were collected in a half sphere with radius up to $\sin\theta/\lambda$ = 1.189 $Å^{-1}$ (hkl = 822 and 660) of reciprocal space. Normalization of the incident beam intensity was conducted by measuring the intensity of the reference reflection every 5 observed data in order to conquer the current decay of the synchrotron radiation with time. The observed integrated intensities were corrected for the Lorentz and polarization factors. A full matrix least–squares refinement was executed by using the diffraction intensities of 23 crystallographically independent reflections. An absorption correction was made for the integrated

intensity. However, it was extremely small ($\mu r = 2.75 \times 10^{-3}$) because of a very small sample (r = 20 μm) and short wave length.

II–3–2. κ–parameter and anharmonic thermal vibration

II–3–2–1. κ–refinement

As mentioned in Chapter 1, for a first approximation the charge density distribution described by its atomic scattering factor is approximated to be a convolution of isolated–atoms. For a simple improvement beyond this isolat–ed–atom approximation a radial dependence of atomic distribution is allowed to be changed; such a change is analyzed by introducing a change in the radial dependence of the atomic scattering factor. This approach is called "κ refinement", which is proposed by Coppens *et al.* (1979) and van der Wal & Stewart (1984).

The following atomic scattering factor (f) of C atoms which was modified from Hartree–Fock calculation for the isolated atom model was accounted for the refinement:

$$f(S/2) = fC^{4+}(S/2) + fC^{2+}–C^{4+}(S/2\kappa) + pfC^{0}–C^{2+}(S/2\kappa) + f' + if'', \qquad [2.3.2.1.1]$$

where $S = 2\sin\theta/\lambda$; κ is a parameter of radial distribution of electron in wave function; p is an occupancy parameter of scattering factor for core and valance electron; fC^{4+} can be assigned to the atomic scattering factor (f) of the core electrons of the carbon atom; fC^{0} represents f of the total electron of non–ionic atom; fC^{2+} does f of 2s and 1s electrons; $fC^{2+}–C^{4+}$ is defined by $fC^{2+} - fC^{4+}$; f' and f'' are the anomalous dispersion terms. In the present

refinement in consideration of the charge density distribution due to covalent sp^3 hybridization, $f(S/2)$ is given by:

$$f(S/2) = fC^{4+}(S/2) + fC^{0}-C^{4+}(S/2\kappa) + f' + if''. \qquad [2.3.2.1.2]$$

II–3–2–2. Anharmonic thermal vibration and anharmonic thermal parameter

Anharmonic thermal vibration in solids explains some inconsistencies of the 'harmonic approximation' as: the deficiency of Dulong–Perit's law for the temperature dependence of heat capacity at high temperature; the temperature dependence of volume *i.e.* thermal expansion.

Thermal conduction in electrical insulator or semi–conductor is due to phonons mainly and is restricted by the anharmonicity in thermal vibration of atoms; the site symmetry for atoms in diamond crystal allows asymmetric anharmonic vibration.

Anharmonic thermal motion of an atom is also treated through the probability distribution function, P(**u**) of the atom, where **u** is a displacement from its equilibrium position; this introduces anharmonic terms with higher order in the temperature factor. The deviations from harmonic thermal motion of carbon atoms were considered by *anharmonic temperature factors*. In this study the anharmonic thermal motion is analyzed by the following 3–dimensional Gram–Charlier expansion (Johnson & Levy (1974)) of the trivariate Gaussian probability density function:

$$T(\mathbf{h}) = \exp(-\beta_{pq}h_ph_q)[1 + \{(2\pi i)^3/3!\}c_{pqr}h_ph_qh_r + \{(2\pi i)^4/4!\}d_{pqrs}h_ph_qh_rh_s + ...], \qquad [2.3.2.2.1]$$

where β_{pq} denotes the anisotropic harmonic temperature factor and h indi–

cates the reflection indices.

T(**h**) is expressed by the Fourier transform of the probability density function of atom, P(**u**):

$$T(\mathbf{h}) = \int P(\mathbf{u})\exp(2\pi i\mathbf{h}\cdot\mathbf{u})d\mathbf{u}. \qquad [2.3.2.2.2]$$

The relation between probability density P(**u**) and the effective one-particle potential (OPP), V(**u**), can be derived from statistical thermodynamics (Dawson & Willis (1967); Willis (1969)). V(**u**) for the cubic symmetry is expressed by:

$$V(\mathbf{u}) = V_0 + 1/2\cdot\alpha\mathbf{u}^2 + \beta u_1u_2u_3 + \gamma\mathbf{u}^4 + \delta(u_1^4 + u_2^4 + u_3^4 - 3/5\mathbf{u}^4). \qquad [2.3.2.2.3]$$

where α, β, γ and δ are called as "anharmonic potential parameters". In addition P(**u**) is expressed by V(**u**), as follows:

$$P(\mathbf{u}) = \exp[-V(\mathbf{u})/k_BT]/\int \exp[-V(\mathbf{u})/k_BT]d\mathbf{u}, \qquad [2.3.2.2.4]$$

where k_B is the Boltzamnn constant; $\mathbf{u}^2=(u_1^2+u_2^2+u_3^2)$.

In the present study anharmonicity of diamond structure at room temperature shows a small deviation from the harmonic potential. Then the following approximation proposed by Dawson & Wills (1967) and modified by Mair *et al.* (1974) was applied to $\exp[-V(u)/k_BT]$ using $e^x \approx 1 + x$, when x is much smaller than unity:

$$\exp[-V(u)/k_BT] = \exp(-i^2\alpha/2k_BT\cdot\mathbf{u}^2)[1 - i^3\beta/k_BT\cdot u_1u_2u_3 + i^4\gamma/k_BT\cdot\mathbf{u}^4 + i^4\delta/k_BT\cdot(u_1 + u_2 + u_3 - 3/5\cdot\mathbf{u}^4)]. \qquad [2.3.2.2.5]$$

The anharmonic potential parameters are introduced from eq's. [2.3.2.1.4] and [2.3.2.1.5] into the temperature factor, T(**h**)

II–3–2–3. Refinement procedure

Firstly the conventional least–squares refinement included only an anisotropic temperature factor β_{ij} and isotropic extinction parameter G_{ex}. The isotropic extinction parameter was refined on the basis of the type I model (Becker & Coppens, 1974). The present investigation requires the precise refinement of the static electron density of carbon atoms and their thermal motion in diamond structure. In the least–squares calculation, parameters estimating anisotropic valence electron distribution have strong correlations with parameters describing the thermal atomic motion. Therefore, in the first stage the electron distribution adopted a monopole model in disregard of the anharmonicity of the thermal motion. Charge density of valence electron was elucidated by κ–refinement (Coppens et al., 1979; van der Wal, 1984) on the basis of the structure factor F(hkl). In the second stage the deviations from harmonic thermal motion of carbon atoms was considered for temperature factors T(**h**).

III. Results

III–1. Lattice constants

The precise measurement of diffraction angle and profile analysis revealed the difference in the lattice constant with nuclear mass. The lattice constants of the five samples with different isotope ratio were determined using the 2θ data sets for 25 independent reflections as described above, and are listed in Table 3.1.1. The standard deviations of the lattice constants were within the range of 5–9 x 10^{-5} Å.

The variation of lattice constant with the isotope ratio can be expressed by the following linear and quadratic equations:

$$a(X) = 3.56708 - 5.4 \times 10^{-4}X \quad \text{with } R^2 = 0.953, \qquad [3.1.1]$$

$$a(X) = 3.56712 - 9.0 \times 10^{-4}X + 3.7 \times 10^{-4}X^2 \quad \text{with } R^2 = 0.990, \qquad [3.1.2]$$

where the isotope ratio, X, is the fraction of $X = [^{13}C]/([^{12}C]+[^{13}C])$ and R is the goodness–of–fit (GoF) index in the least–squares calculation, where R is determined as:

$$R = \frac{n\cdot\Sigma a_i X_i - \Sigma a_i \cdot \Sigma X_i}{\sqrt{\{n\cdot\Sigma a_i - (\Sigma a_i)^2\}}\cdot\sqrt{\{n\cdot\Sigma X_i^2 - (\Sigma X_i)^2\}}} \qquad [3.1.3]$$

The GoF index indicates that the quadratic equation is more suitable to describe the variation of the lattice constant. The observed lattice constants are plotted as a function of X in Fig. 3.1.1. and the above quadratic equation, which provides a better fit, is shown as a solid line. The difference between the lattice constant of natural diamond and that of ^{13}C diamond is found to be $\Delta a/a = -1.51 \times 10^{-4}$, which is extremely small and is the same as the value

determined by Holloway *et al.* (1991 & 1992). (Note again that "natural" diamond have the same isotope composition with natural one and "^{13}C" diamond do the composition which is mostly enriched ^{13}C isotope.)

III–2. Difference in the κ–refinement

After the full matrix least–squares refinements including anisotropic thermal parameter and extinction parameter, the reliability factor of the least–squares calculation $R[= \Sigma||Fo| - |Fc||/\Sigma|Fc|]$ was 0.0082 and 0.0098 for natural and ^{13}C diamond, respectively.

At this stage κ–refinement was carried out by introducing the atomic scattering factor as expressed by the equation [2.3.2.1.2]. (Fig.3.2.1.)
κ parameter was refined in full matrix least–squares calculation for both samples. ^{13}C diamond has a larger $\kappa[= 0.993(1)]$ than $\kappa[= 0.931(7)]$ of natural one, which indicates valence electron of natural diamond is more widely distributed than that of ^{13}C diamond. This is probably related to the difference in zero–point motion of the atoms in both diamonds.

III–3. Isotope effect on the anharmonic thermal vibration

The κ–refinement was initiated from the harmonic oscillation model in the full–matrix least–squares procedure. Natural diamond has a little larger anisotropic thermal parameter of β_{11} than ^{13}C diamond. It may possibly be concluded that the parameter is related to the reduced mass.

As shown in Fig. 3.3.1., difference Fourier synthesis on (110) plane based on the harmonic thermal vibration exhibits a considerably large bond–

ing electron density between two carbon atoms for both natural and ^{13}C diamond, which accords well with the theoretical total valence electronic charge density by self-consistent pseudopotential calculation (Denteneer *et al.* (1985); Chelikowsky & Cohen (1974)). This feature of the bonding electron density reveals few difference between natural and ^{13}C diamond. The difference Fourier map shown in Fig. 3.3.1. exhibits the non-spherical residual electron density around the atoms, which is related to the anharmonic thermal vibration of atoms.

The anharmonic thermal parameters up to 4th-rank coefficients were reliable, because the parameters over the 5th-rank have too high correlations with each other to offer the meaningful values. The temperature parameters higher than 4th-rank in the eq.[2.3.2.2.1] were truncated in the present refinement. The converged thermal parameters are presented in Table .3.1.2. The only four thermal parameters of $\beta_{11}(= \beta_{22} = \beta_{33})$, c_{123}, d_{1111} (= d_{2222} = d_{3333}) and $d_{1122}(= d_{1133} = d_{2233})$ are independent variables. The refinement resulted in a slightly larger anisotropic anharmonic thermal vibration of c_{123} of natural diamond than that of ^{13}C. This indicates that the anharmonicity is dominant in the <111> direction. An example of the difference Fourier maps on (110) plane of ^{13}C diamond after the anharmonic refinement is presented in Fig. 3.3.2.

The temperature factors, T(**h**), were measured through these diffraction experiments. Potential parameters of OPP, α, β, γ and δ were calculated from the thermal parameters of β_{11}, c_{123}, d_{1111} and d_{1122} using modified forms of OPP equations proposed by Konito & Stevens (1982) originally, which were

detailed in Yamanaka *et al.* (1984 & 1985). These parameters are presented in Table 3.3.2. The potential curves of ^{13}C in the direction parallel to <111>, <110> and <100> are shown in Fig. 3.3.3. The anharmonic potential curve in the <111> direction shown in Fig. 3.3.4. is compared between natural and ^{13}C diamond.

IV. Discussion

Lattice dynamic study (Chrenko (1988); Hass *et al.* (1992)) reveals that lattice vibration differs between ^{12}C and ^{13}C diamond. This differences and the decreasing trend of the Raman frequency with ^{13}C concentration are explained mainly due to mass difference between isotopes, $\Delta M/M$, namely $\omega \propto \bar{M}^{-1/2}$ from the virtual–crystal approximation.

The fractional unit–cell volumes difference between isotopes in solids composed of single element has been discussed from thermodynamic considerations by London (1958). Buschert *et al.* (1988) proposed the following relation from the equation of state using Helmholtz's free energy for the unit–cell volume change based on the above London theory:

$$\Delta V/V = -1/2V \cdot \Delta M/M \cdot \kappa \Sigma \gamma_i (E_i - C_i T), \qquad [4.1]$$

where κ is the isotherm compressibility, γ_i the Grüneisen constant defined by $\gamma_i = -\partial(\ln\omega_i)/\partial(\ln V)$, E_i the internal energy and $C_i (= dE_i/dT)$ the heat capacity, associated with i–th phonon respectively. Applying the zero–temperature limit, which is justified with reference to the large Debye temperature, Θ, of 2200 K for diamond, to contribution of heat capacity yields the an equation for the difference of the lattice parameter:

$$\Delta a = -3\Delta M/2M \cdot \kappa/a^3 \cdot \Sigma \gamma_i E_i, \qquad [4.2]$$

Holloway *et al.* (1991) obtained $\Delta a/a = -2.1 \times 10^{-4}$ from this equation with an estimated value of $\gamma = 1.1$ in reasonable agreement with -1.5×10^{-4} observed in their diffraction experiment. The possibility of under–estimating must be exist because they use the reported Debye frequency *i.e.* ignore a contribution of optical mode phonon, which is considered in the original

Buschert's work for Ge isotope.

Ramdas *et al.* (1993) proposed another approach for the difference in the lattice parameter taking into account the anharmonicity of the internal potential assuming a simple Einstein model. This should be noted that their internal potential is the same concept of one–particle–potential (OPP) appearing in derivation of the anharmonic temperature factor. The anharmonicity appears in the potential energy of an atom:

$$V(u) = (\alpha_v/2)u^2 - (\beta_v/6)u^3 + \ldots \qquad [4.3]$$

where u is displacement from the equilibrium position, α_v and β_v are positive constant. They only considered up to 3rd order and gives the following relation for the lattice parameter:

$$a = a_B + (\hbar\beta_v/4\alpha_v)(\alpha_v M)^{-1/2} \qquad [4.4]$$

where a_B is the value on the absence of zero–point motion. The important consequence of this equation is the lattice parameter depends on the 3rd order anharmonic parameter, β_v, as well as do on the mass of the atom, M. This is not confused with eq.[4.1] and [4.2] which seem not depend on any anharmonic term because the Grüneisen parameter *i.e.* the dependence of volume on frequencies is result of such anharmonicity in the potential for an atom.

Raman peak–shift previously observed as a function of isotope composition in diamonds confirms that the frequency ratio $\omega(X)^2/\omega(0)^2$ in the whole solid solution range was not simply varied in a linear relation with the isotope content (X). The non–linear change of the ratio is coincident with the variation of the lattice parameter taking into account of the dependence on the anharmonicity mentioned above. The large charge density in the middle of

covalent C–C bonding, which is clearly shown in difference Fourier map (*e.g.* Fig. 3.3.2), should cause anharmonic thermal of atom in a fashion favoring the direction contrary to the bond; this study reveals such an anharmonicity of thermal motion of C atoms in diamond.

As shown Fig. 4.1., the unit–cell volume difference between natural and ^{13}C diamond is on the line with those of the crystals composed of single element with various isotope ratio. As seen in eq.[4.4], the lattice parameter change caused by substitution of isotope has been explained by the fractional mass ratios $\Delta M/M$ of isotopes and the anharmonic thermal vibration of atoms. (London (1958); Buschert *et al.*(1988); Ramdas *et al.* (1991)).

The observed anharmonic coefficients of d_{1111} and d_{1122} are indeed small and the order of 10^{-8}, however, c_{123} is in the order of 10^{-6}; This indicates that the anharmonicity in thermal vibration is still large enough to be considered even at room temperature where far below the Debye temperature of 2200 K of diamond. On the derived anharmonic potential parameters, the positive large value of 3rd order β in contrast to small γ and δ for 4th order suggests anharmonic thermal vibration of atoms is enhanced in the direction to $\langle\bar{1}\ \bar{1}\ \bar{1}\rangle$; both isotropic and anisotropic 4th–order anharmonicity is quite small. At the higher temperature 4th–order term must be large otherwise the potential will be diverse only 3rd–term; below the room temperature, OPP should be described well within the 3rd–term for both natural and ^{13}C diamonds. Both difference Fourier map shown in Fig. 3.1.1. and anharmonic potential curve in Fig. 3.3.4. indicate that the anharmonicity is dominant in the <111> direction.

The κ–refinement reveals that valence electrons tend to contract to the nucleus in ^{13}C diamond comparing with that in the natural. This should be strikingly affects on the smaller lattice parameter of ^{13}C diamond.

Note that Yamanaka *et al.* (1984 & 1985) reported the anharmonic thermal motion focused on the atoms having the site symmetry of $\bar{4}3m$, which is the same of the carbon in the diamond structure, in the systems of $MgAl_2O_4$ with the spinel structure and ZnX (X=S, Se, Te) with zinc blende structures. The refinements for these both systems reveal a large anharmonic–ity of cations in the $\bar{4}3m$ site. These compounds have the ionic bonding character. However, the covalent character in diamond causes the residual electron density around atoms which is different from those of $MgAl_2O_4$ and ZnX.

Although the extremely high Debye temperature (2200 K) and large stiffness tensors of elastic constants, c_{11} = 1097 ± 5, c_{12} = 124 ± 5, and c_{44} = 578 ± 2 GPa (McSkimin & Andreatch (1972)) and a remarkably small ther–mal expansion coefficient of 0.81 x 10^{-6} K^{-1} (Slack & Bartram (1975)), this diffraction study on diamonds reveals electron density distribution and anharmonicity in thermal vibration of atoms and isotope effects on them using a set of structure factors with large value of $\sin\theta/\lambda$.

References

Angus, J. C. & Hayman, C.C. (1988). *Science* **241**, 913–21.

Anthony, T. R., Banholzer, J., Fleischer, Wei, L. Kuo, P. K., Thomas, R. L. & Pryor, R. W. (1990). *Phys. Rev. B* **42**, 1104.

Benholzer, W. F. & Anthony, T. R. (1992). *Diamond Relat. Mater.* **1**, 1157–60.

Banholzer, W. F., Anthony, T. R. & Gilmore, R. (1992). *New Diamond Science and Technology* p.857, MRS Int. Conf. Proc.

Berezin, A. A. & Ibrahim, A. M. (1988). *Mater. Chem. Phys.* **19**, 407.

Bolz, L. H. & Maner, F. A. (1962). *Adv. X–ray Anal.* **6**, 242.

Bond, W. L. (1960). *Acta Crystallogr.* **13**, 814.

Brill, R., Grimm, H. G., Hermann, C. & Peters, C. (1939). *Ann. Phys. (Leipzig)* **34**, 393–445.

Buschert, R. C., Merlini, A. E., Pace, S., Rodriguez, S. & Grimsditch, M. H. (1988). *Phys. Rev. B* **38**, 5219–21.

Chelikowsky, J. R. & Cohen, M. L. (1974). *Phys. Rev. Lett.* **33**, 1339–42.

Chrenko, R. M. (1988). *J. Appl. Phys.* **63**, 5873–5.

Coington, E. J. & Montgomery, D. J. (1957). *J. Chem. Phys.* **27**, 1030.

Collins, T. A., Lawson, S. C., Davies, G. & Kanda, H. (1990). *Phys. Rev. Lett.*

Coolins, T. A., Davies, G., Kanda, H. & Woods, G. S. (1988). *J. Phys. C* **21**, 1363–76.

Coppens, P., Guru Row, T. N., Stevens, E. D., Becker, P. J. & Yang, Y. W. (1979). *Acta Crystallogr.* **A35**, 63–72.

Dawson, B. (1967). *Proc. R. Soc. London Ser. A* **298**, 264–88.

Dawson, B. (1975). *Adv. Struct. Res. Diffr. Methods* **6**, 1–250.

Dawson, B. & Sanger, P. L. (1967). *Proc. R. Soc. London Ser. A* **301**, 195–209.

Dawson, B. & Willis, B. T. M. (1967). *Proc. R. Soc. London Ser. A* **298**, 307–15.

Denteneer, P. J. H. & van Haeringen, W. (1985). *J. Phys. C* **18**, 4127–42.

Deutsch, M. & Hart, M. (1985). *Acta Crystallogr.* **A41**, 48–55.

Göttlicher, S. & Wölfel, W. (1959). *Z. Electrochem* **63**, 891.

Hass, K. C., Tamor, M. A., Anthony, T. R. & Banholzer, W. F. (1992). *Phys, Rev. B* **45**, 1104.

Hass, K. C., Tamor, M. A., Anthony, T. R. & Banholzer, W. F. (1991). *Phys. Rev. B* **45**, 7171–82.

Holloway, H., Hass, K. C., Tamor, M. A., Anthony, T. R. & Banholzer, W. F. (1991). *Phys. Rev. B* **44**, 7123–6; (1992). *Phys. Rev. B* **45**, 6353(E).

Johnson, C. K. & Levy, H. A. (1974). *"International Tables for X–ray Crystallography Vol. IV"*, pp.311–36, Birmingham; Kynoch Press.

Kanda, H., Ohsawa, T., Fukunaga, O. & Sunagawa, I. (1989). *J. Cryst. Growth* **94**, 115–24.

Kogan, V. S. & Bulatov, A.S. (1962). *Sov. Phys. JETP* **15**, 1041.

Kontio, A. & Stevens, E. D. (1982). *Acta Crystallogr.* **A38**, 623–9.

Kotani, T. & Yamanaka, T. (1991). *Phys. Rev. B* **44**, 6131–6.

Kurki–Suonio, K. & Ruuskanen, A. (1971). *Ann. Acad. Sci. Fenn. Ser. A6* **308**, 1–29.

London, H. (1958). *Z. Phys. Chem. Neue. Folge* **16**, 302–9.

Mair, S. L., Barnea, Z., Cooper, M. J. & Rouse, K. D. (1974). *Acta Crystallogr.* **A30**, 806–13.

Mair, S. L. & Wilkins, S. W. (1976). *J. Phys. C* **9**, 1145–58.

McConnell, J. F. & Sanger, P. L. (1970). *Acta Crystallogr.* **A36**, 83–93.

McSkinmin, H. J. & Andreatch, P. (1972). *J. Appl. Phys.* **43**, 2944–8.

Nishida, Y., Yamada, Y., Umezawa, N., Hanzawa, H., Kobayashi, M., Kanda, H. & Nasajima, T. (1992). personal communication.

Price & Maslen (1978). *Acta Crystallogr.* **A34**, 173–83.

Ramdas, A. K., Rodriguez, S., Grimsditch, M., Anthony, T. R. & Banholzer, W. F. (1993). *Phys. Rev. Lett.* **71**, 189–92.

Renninger, M. (1955). *Acta Crystallogr.* **8**, 606–10.

Sakamaki, T., Hosoya, S., Tagai, T., Ohsumi, K. & Satow, Y. (1984). *J. Appl. Crystallogr.* **17**, 219–225.

Sasaki, S. (1989). *Rev. Sci. Instrum.* **60**, 2417–20.

Slack, G. A. & Bartram, S. F. (1975). *J. Appl. Phys.* **46**, 89–98.

Spackman, M. A. (1991). *Acta Crystallogr.* **A47**, 420–7.

Stewart, R. F. (1973a). *Acta Crystallogr.* **A29**, 602–5.

Stewart, R. F. (1973b). *J. Chem. Phys.* **58**, 4430–8.

Strong, H. M. & Wentorf, R. H. (1991). *Am. J. Phys.* **59**, 1005–8.

Takama, T. & Sato, S. (1988). *Aust. J. Phys.* **41**, 433–48.

Tischler, J. Z. & Batterman, B. W. (1984). *Phys. Rev. B* **30**, 7060–6.

van der Wal, R. J. & Stwart, R. F. (1984). *Acta Crystallogr.* **A40**, 587–93.

Weiss, R. J. (1964). *Phys. Lett.* **12**, 293–5.

Weiss, R. J. & Middleton, R. (1965). priveate communication to Dawson (1967).

Wilkis, J. (1967). *"The properties of Liquid and Solid Helium"* 678–9., Clarendon, Oxford.

Willis, B. T. M. (1969). *Acta Crystallogr.* **A25**, 227–300.

Yamanaka, T., Takeuchi, Y. & Tokonami, M. (1984). *Acta Crystallogr.* **B40**, 96–102.

Yamanaka, T., Takeuchi, Y. & Tokonami, M. (1985). *Acta Crystallogr.* **B41**, 298–304.

Young, R. A. & Wiles, D. B. (1982). *J. Appl. Crystallogr.* **15**, 430–8.

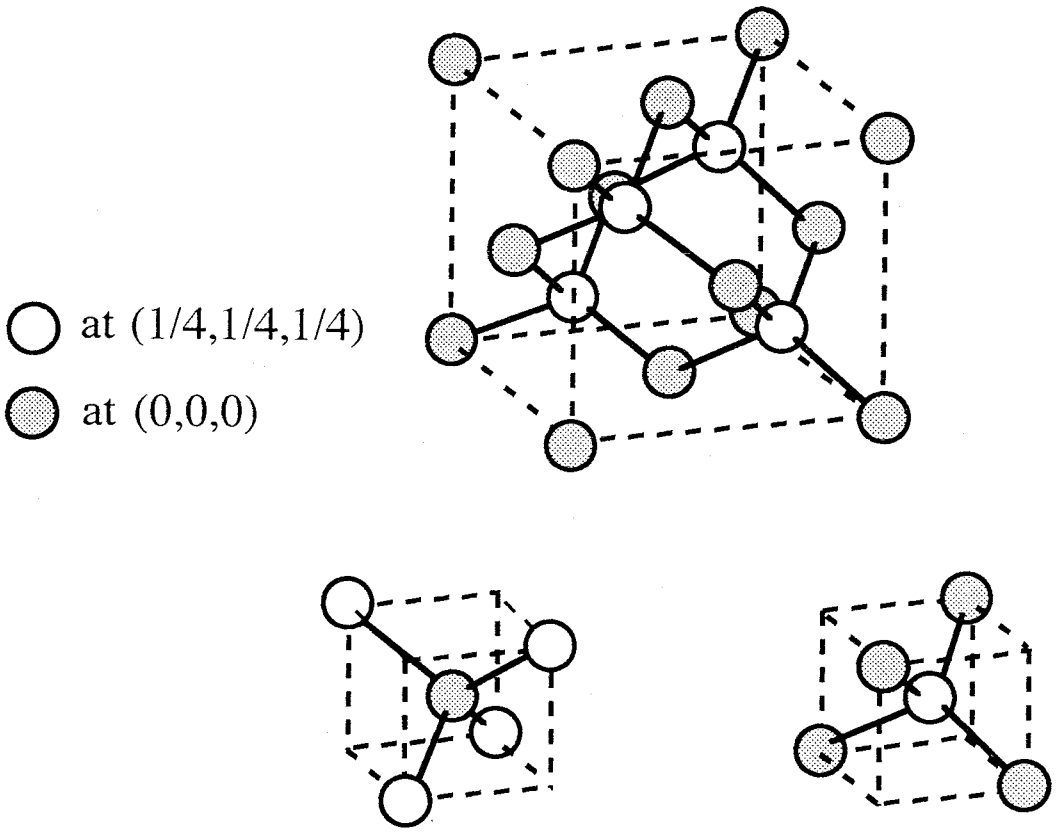

Fig. 1.1. Diamond strucutre (upper) and two types of atomic configuration in diamond strucuture (lower); the center of symmetry is at (1/8,1/8,1/8).

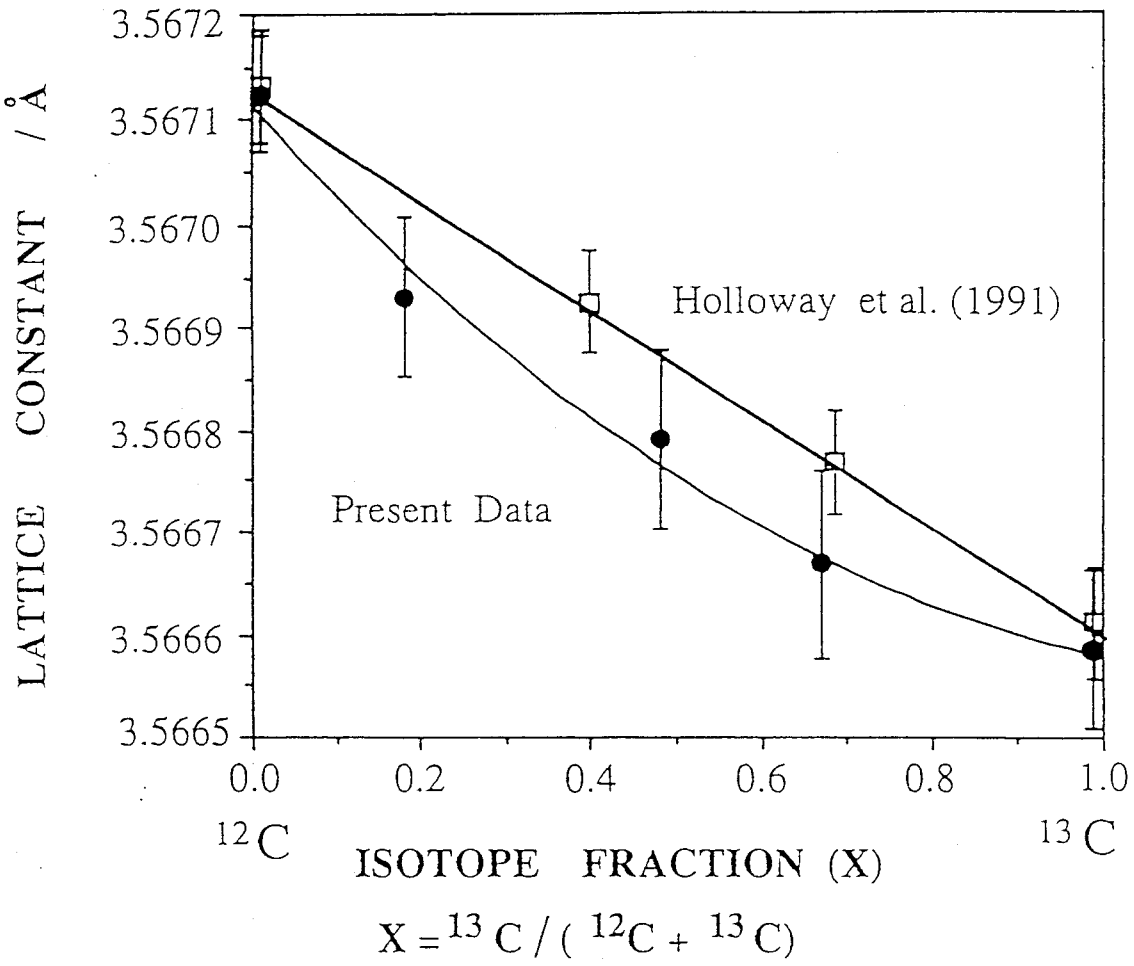

Fig. 3.1.1. Isotope dependence of the lattice constant of diamond. The curved line shows the quadratic equation [3.1.2] which fits to solid circles obtained in the present work. The present compositional error is smaller than the solid circle. The straight line fits to open squares those obtained by Holloway *et al.* (1991 & 1992)

Table 3.1.1. Lattice constant of $^{13}C_x{}^{12}C_{(1-x)}$ diamond

X	a(A)	V(A^3)	V/Vo	d(A)
0.02(1)	3.56712(5)	45.389	1.00000	1.54460(2)
0.18(1)	3.56693(8)	45.381	0.99981	1.54452(3)
0.48(1)	3.56679(9)	45.374	0.99966	1.54446(4)
0.67(1)	3.56667(9)	45.371	0.99958	1.54440(4)
0.985(4)	3.56658(7)	45.369	0.99954	1.54436(3)

X indicates the isotope ratio $^{13}C/(^{12}C+^{13}C)$.
V/Vo is the volume ratio, based on the cell volume of natural sample.
d denotes the C–C bond length.
The number in parenthesis is a standard deviation in the last digit.

Table 3.1.2. Analysis of anharmonic thermal parameters

	natural diamond	^{13}C diamond
^{13}C conc.	2.0(8)%	98.5 (4)%
lattice Const(Å)	3.56712(5)	3.56658(7)
vol. (Å^3)	45.3892(1)	45.3686(2)
R(F)	0.78 %	0.88 %
wR(F)	0.81 %	1.40 %
No. of data	23	23
B_{iso}	0.090(2)	0.146(4)
$\bar{u}^2$	0.036	0.043
κ-parameter	0.931(7)	0.993(1)
$G_{iso}x10^{-4}$	0.273(19)	0.210(11)
$\beta_{11}x10^5$	177(41)	287(69)
$c_{123}x10^7$	-57(35)	-41(38)
$d_{1111}x10^8$	-0.7(7)	-0.8(7)
$d_{1122}x10^8$	13(10)	21(13)
$\alpha x10^{20}$ J/Å^{-2}	18.62	11.36
$\beta x10^{20}$ J/Å^{-3}	10.21	1.668
$\gamma x10^{20}$ J/Å^{-4}	- 1.301	- 0.3953
$\delta x10^{20}$ J/Å^{-4}	- 3.467	1.0222

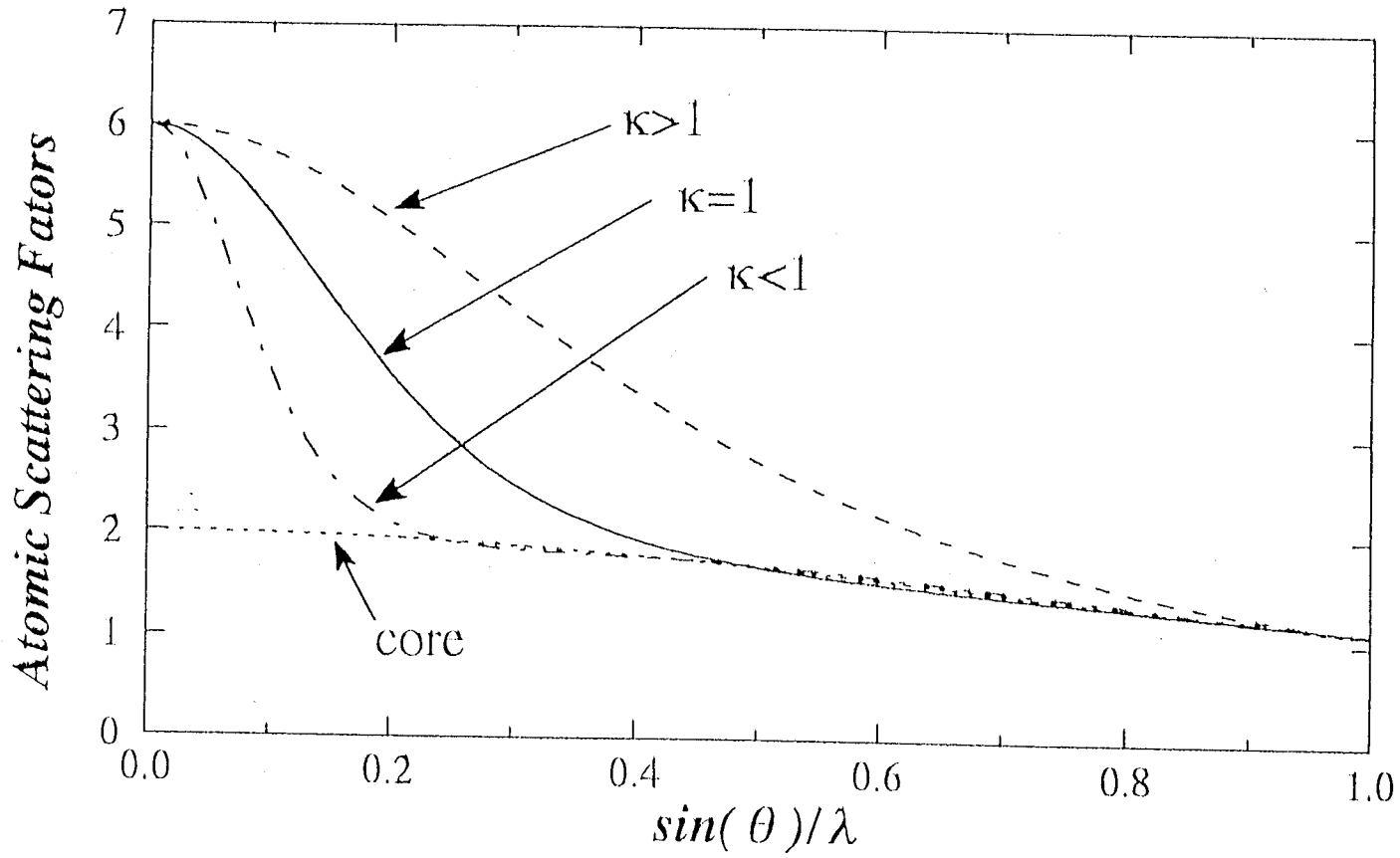

Fig. 3.2.1. Schematic representation of atomic scattering factors: for core (fC^{2+}), for $\kappa<1$, $\kappa=1$ and $\kappa>1$.

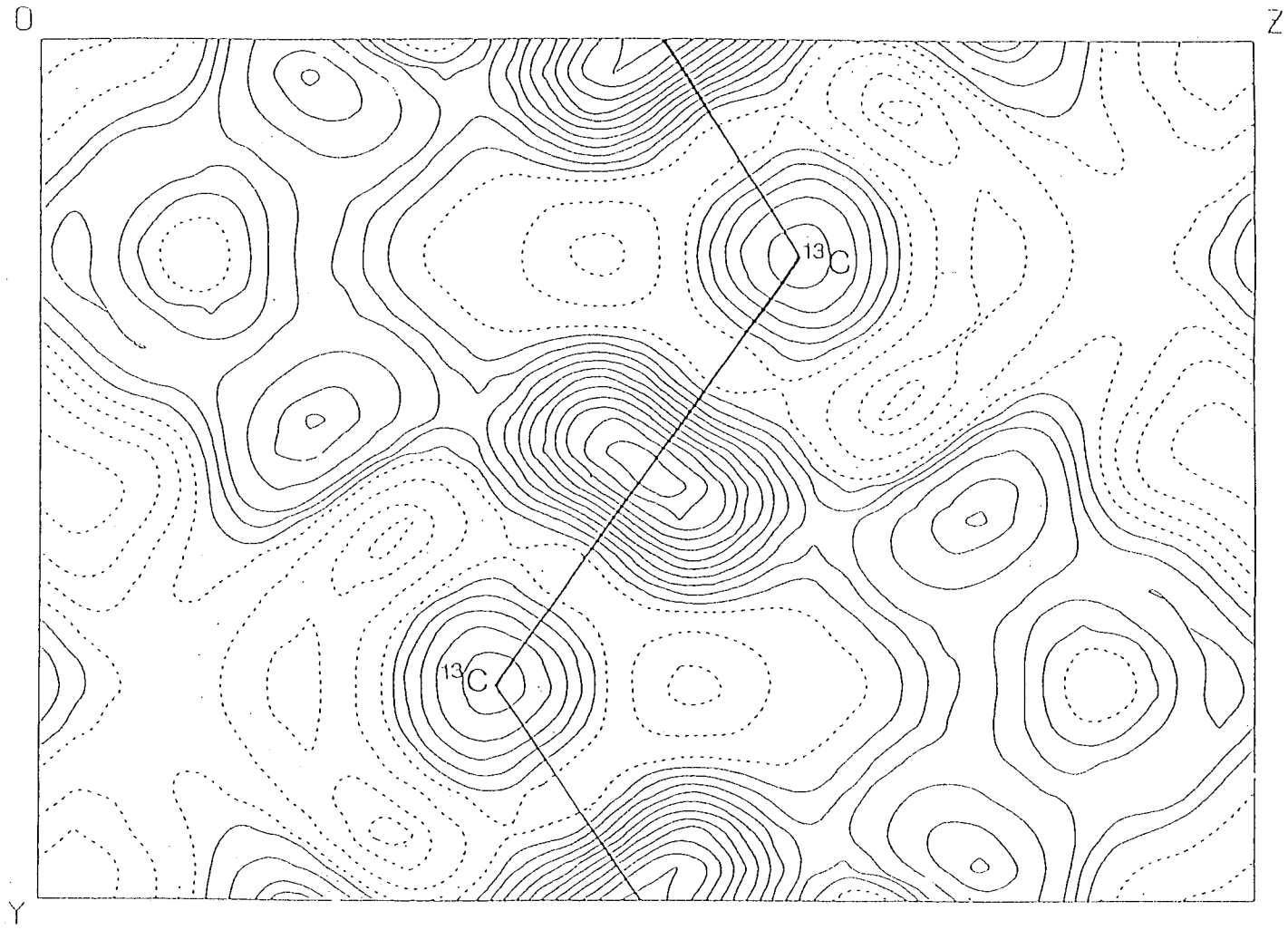

Fig. 3.3.1. Difference Fourier map of ^{13}C diamond onto (110) after the refinement of harmonic theramal parameter and κ–refinement. A unit contour is 0.02e/Å^3. The map reveals the bonding electron and residual electron density around the atoms, which is related to the anharmonic thermal vibration atoms.

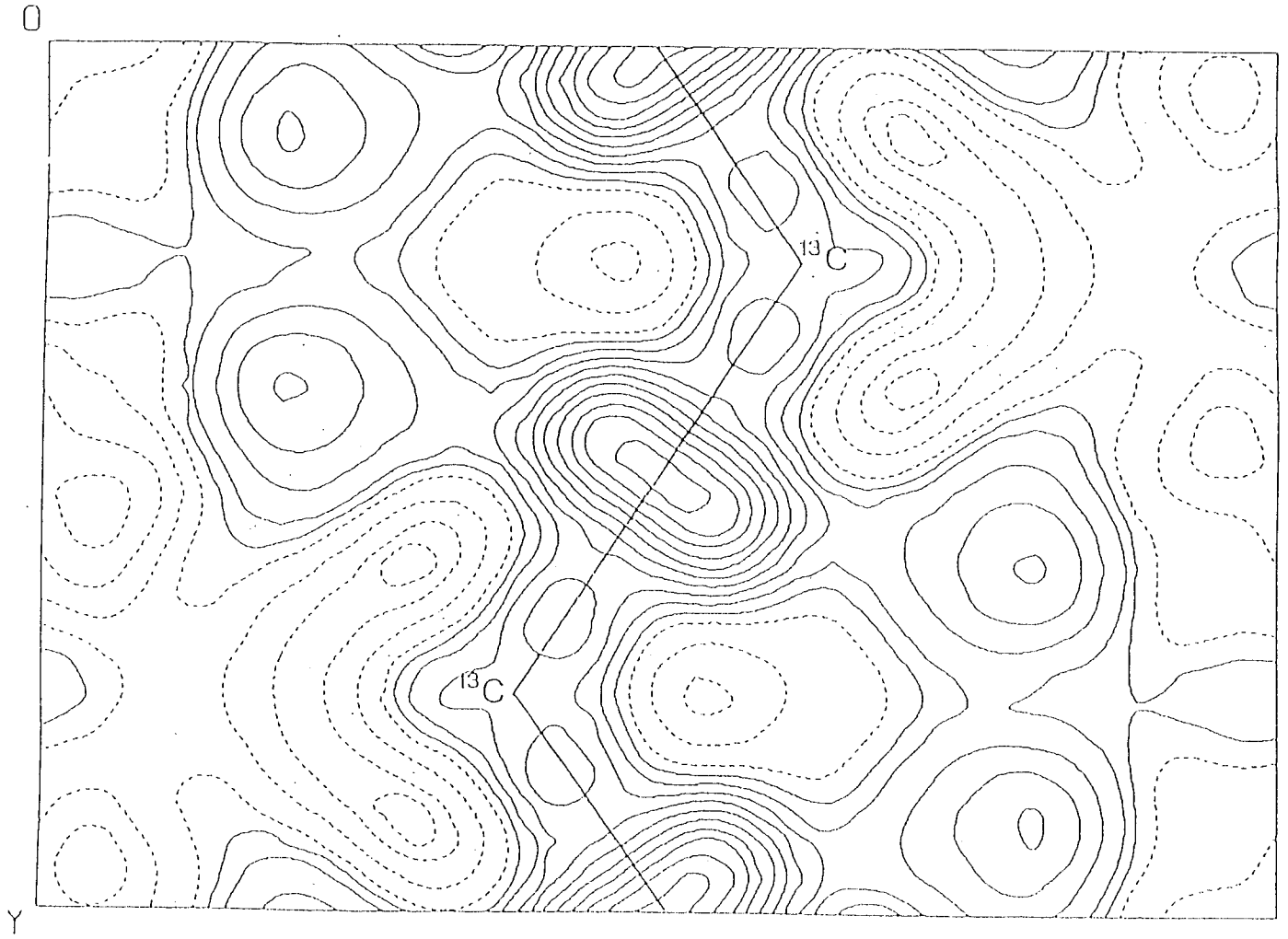

Fig. 3.3.2. Difference Fourier map of ^{13}C diamond onto (110) after the refinement of the anharmonic thermal vibration. A contour interal is same as that in Fig. 3.3.1.

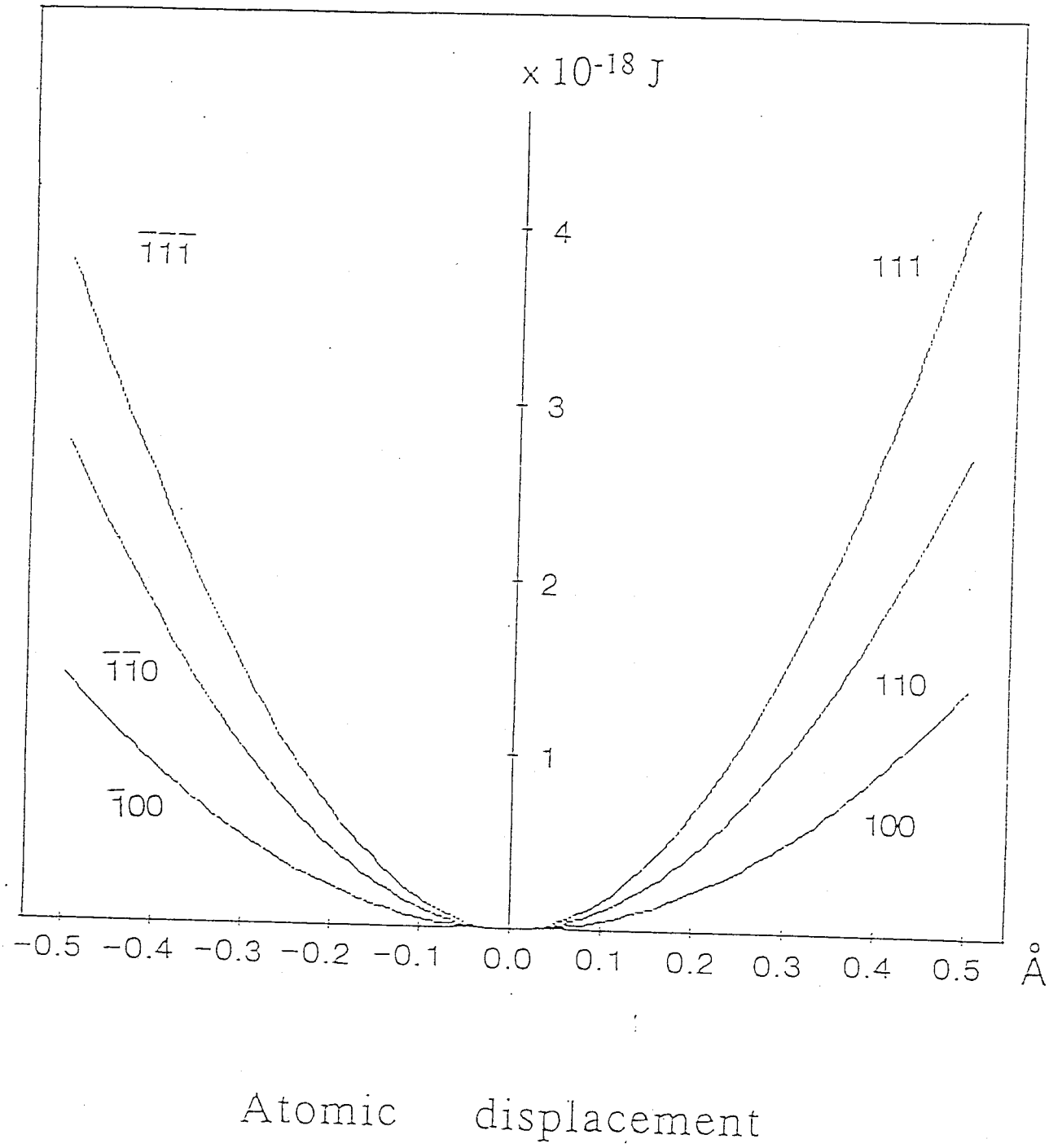

Fig. 3.3.3. Anharmonic potential of ^{13}C diamond in the direction parallel to <100>, <110> and <111>. Anisotropic anharmonisity in the atomic viobrational potential is observed only in the direction of <111>.

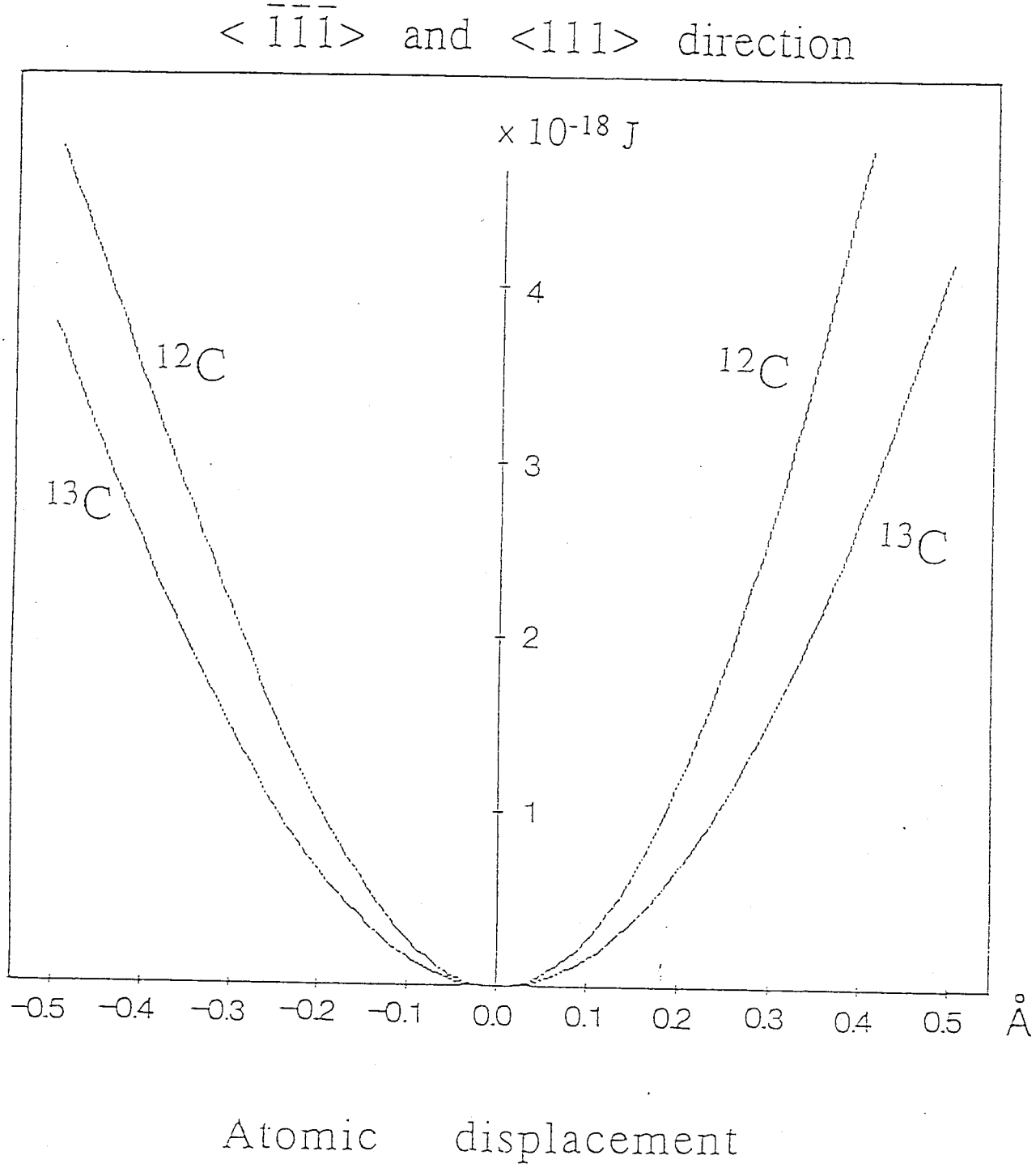

Fig. 3.3.4. Anharmonic potential curve in the <111> and <111> direction of natural and ^{13}C diamond.

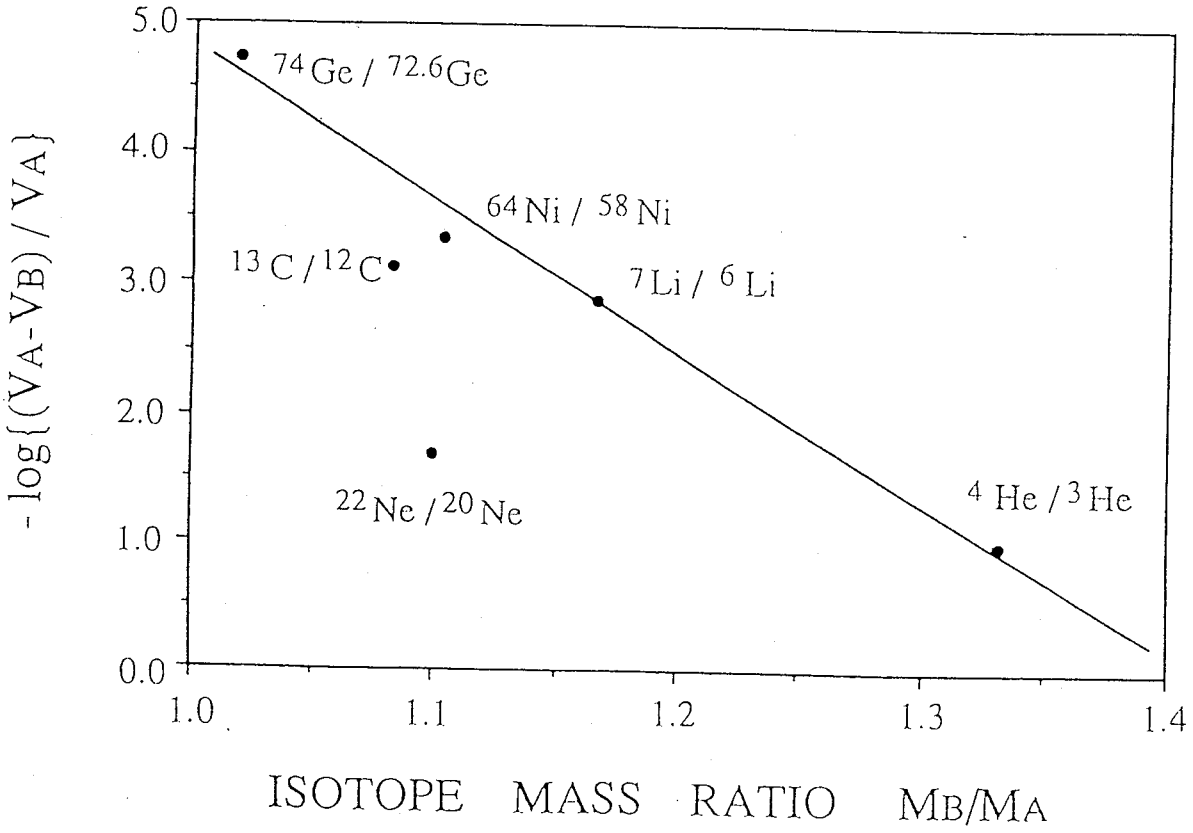

Fig. 4.4.1. Cell volume difference of crystals composed of single element with different isotopes. The volume differences are plotted as a function of the mass ratio of solids composed of one element

Chapter 4. SUMMARY

X-ray diffraction studies using synchrotron radiation (SR) are applied to $CaFeO_3$ both in "non-charge-disproportionate" state and in charge-disproportionate state, and diamonds with various concentration of ^{13}C isotope.

The study on $CaFeO_3$ is summarized as follows:

(1) The cube-shaped crystalline samples of $CaFeO_3$ containing Fe^{4+} with edge size of 0.06 mm were synthesized under 3 GPa and at around 1273 K by the help of CaO_2 as an oxidizer.

(2) $CaFeO_3$ was revealed to have a same structure as $GdFeO_3$ with Pbnm at 293 K [Z = 4, a = 5.3480(3), b* = a, c = 7.5730(5) Å].At 113 K, Fe^{3+} and Fe^{5+} are suggested to arrange NaCl type sub-lattice of Fe. Thereby the space group at 113 K is resulted to be monoclinic $P2_1/n$ [Z = 4, a = 5.3409(3), b* = a, c = 7.5585(13) Å, $\beta^* = 90°$] which is one of sub-groups of Pbnm. (* coincidence within experimental error)

(3) The smaller bond angle (*ca.* 160°) of Fe-O-Fe in $CaFeO_3$ than that in $SrFeO_3$ are observed. This suppresses an itinerant nature of e_g(Fe) electron and causes "disproportionation" at low temperature instead of "Jahn-Teller distortion".

(4) FeO_6 octahedra in almost regular shape at RT and 113K are explained as follows: at RT, 3d electrons of Fe^{4+} delocalize to reduce Jahn-Teller effect; at 113K, Fe^{4+} is "disproportionated" into Fe^{3+} (half filled t_{2g} and e_g) and Fe^{5+} (half filled t_{2g}) without any distortion of FeO_6.

(5) Large residual electron density peaks with 1.2e/Å^3 as a maxima are should be strong covalent contribution of an overlapping of e_g(Fe) orbital and 2p(O) one.

The studies on the diamonds with various concentration of ^{13}C isotope are summarized as follows:

(1) The SR X-ray diffraction studies using small and approximately sphere samples of 0.02 mm reveal differences due to isotope concentration in the lattice constants, charge density distributions around atoms caused by covalent bonds, and thermal vibrations of atoms.

(2) Applications of the refinements of κ-parameter and the anharmonic thermal parameters apparently reduce the residual electron densities around atoms after the refinements in both natural and ^{13}C diamond. The positiveness of these refinements is demonstrated.

(3) The precise measurement of diffraction angle and profile analysis revealed the differences in the lattice constant with nuclear mass. The variation of lattice constant with the ^{13}C isotope ratio can be expressed by the following quadratic equation:

$$a(X) = 3.56712 - 9.0 \times 10^{-4}X + 3.7 \times 10^{-4}X^2$$

where the isotope ratio, X, is the fraction of $X = [^{13}C]/([^{12}C]+[^{13}C])$. The difference between the lattice constants of natural diamond and ^{13}C diamond is found to be $\Delta a/a = -1.51 \times 10^{-4}$.

(4) κ parameter refinements reveal that ^{13}C diamond has a larger κ[= 0.993(1)] than κ[= 0.931(7)] of natural one. This indicates valence electron of natural diamond is more widely distributed than that of ^{13}C diamond. This should be strikingly affects on the smaller lattice parameter of ^{13}C diamond.

(5) The anharmonic potential parameters are derived from the observed

anharmonic thermal parameters. The positive large value of 3rd order β in contrast to small γ and δ for 4th order suggests anharmonic thermal vibration of atoms is enhanced in the direction to $< \bar{1}\ \bar{1}\ \bar{1} >$. The 3rd anharmonic potential parameter of γ of natural diamond is revealed to be slightly larger than that of ^{13}C diamond.

LIST of the SUBMITTED PAPERS RELEVANT to THIS THESIS

Yamanaka, T., Morimoto, S. & Kanda, H. (1994). *"Influence of isotope ratio on the lattice constant of diamond", Phys. Rev. B* **49**, 9341–9343.

Yamanaka, T. & Morimoto, S. (1996). *"Isotope effect on anharmonic thermal atomic vibration and* κ *refinement of* ^{12}C *and* ^{13}C *diamond, Acta Crystallogr.* **B52**, in press.